Title: In-situ shear modulus reduction with strain in stiff fissured clays and weathered mudstones

Authors:

Kevin M. Briggs*, HS2 Ltd / RAEng Senior Research Fellow in Geotechnical Engineering, University of Bath, UK.

Yuderka Trinidad González, Assistant Professor, Department of Civil, Construction, and Environmental Engineering, Iowa State University, Ames, IA, United States.

Gerrit J. Meijer, Lecturer in Geotechnical Engineering, University of Bath, UK.

William Powrie, Professor of Geotechnical Engineering, University of Southampton, UK.

Simon Butler, Senior Project Engineer, HS2 Ltd (seconded from Atkins), Birmingham, UK.

Nick Sartain, Head of Geotechnics, HS2 Ltd, Birmingham, UK.

ORCID: KMB, 0000-0003-1738-9692; YATG, 0000-0003-3715-9712; GJM, 0000-0002-2815-5480; WP, 0000-0002-2271-0826.

*Corresponding author: k.m.briggs@bath.ac.uk

Abstract

The non-linear stress-strain behaviour of stiff clays and weak rocks at small and medium strains may be a critical consideration in the design of geotechnical structures. Empirical methods have been developed for estimating the maximum shear modulus and the normalised shear modulus reduction with strain of fine-grained soils. These are usually expressed as functions of the void ratio (or specific volume) and average effective (confining) stress, based on results from laboratory tests. However, the fidelity of these equations has not been widely evaluated in-situ.

This paper describes the use of in-situ measurements from an instrumented embankment to calculate the operational in-situ shear modulus of the underlying stiff clays and weathered mudstones at medium and large strains. It is shown that the shear modulus at very small strain of the weathered clays increased linearly with depth, consistent with empirical equations. The gradient of the normalised, non-linear stiffnesses of the clays were comparable with those measured in laboratory tests of fine-grained soils, at a range of strains. However, the values for the reference strain, where the maximum shear modulus reduces by 50%, were lower than was predicted by the empirical equations. Keywords: stiff clay, weathered mudstone, small-strain stiffness, instrumentation

Introduction

The stress-strain behaviour of stiff clays and weak rocks is highly non-linear (Jardine et al. 1984; Atkinson 2000; Clayton 2011; O'Brien et al. 2023). Their stiffness reduces most rapidly with strain over the medium strain range of 0.001% to 0.1%. This corresponds to typical strain levels around geotechnical structures such as foundations, retaining walls and tunnels, which may vary from small (<0.001%) to large (up to 1%) prior to yield (Jardine et al. 1986; Mair 1993; Clayton 2011).

The reduction of in-situ ground stiffness at small, medium and large strains has been inferred from back-analyses of structural behaviour (Burland 1989; Ng et al. 1995; Ng et al, 1998; Clayton 2011) and is now an important design consideration for the serviceability of many geotechnical structures (BSI 2004; O'Brien et al. 2023). Figure 1 (adapted from Mair 1993; Ishihara 1996; Atkinson 2000 and Clayton 2011) shows the typical reduction in shear modulus (G) from a maximum value (G_{max}) at small strain (<0.001%) towards a lower modulus value at larger strains. The typical ranges of shear strain associated with common in-situ and laboratory testing methods, and applicable to geotechnical analyses, are also indicated.

Small strain stiffness can be measured using in-situ geophysical tests and in the laboratory using bender elements or resonant column apparatus (Clayton 2011). Stiffness at larger strains can be obtained from conventional and specialist triaxial testing of laboratory samples (Atkinson 2000; Clayton 2011) or from the back-analyses of structural behaviour at full-scale (Burland 1989; Menkiti et al. 2004; Kelly et al. 2018; Smith et al. 2018; Le et al. 2023). However, Hight et al. (2007) and O'Brien et al. (2023) describe a number of practical challenges related to the measurement of non-linear stiffness. For laboratory tests these include the potential for sample disturbance, the slow rate of testing and a limited number of samples or preferential sampling not representing the in-situ geological variation. For in-situ tests or back-analyses, challenges include the high cost, limited range of strain measurement and the relevance of the direction of measurement to that of the design loading. The maximum modulus (G_{max}) from field measurements is often greater than that measured in the laboratory (Tatsuoka et al. 2003; O'Brien et al. 2023). There is also a 'data gap' between measurements of G_{max} at very small strain (<0.001%) and measurements of G in routine laboratory testing, which become less reliable below 0.01% strain. Additional complexities include stiffness anisotropy (Lings et al. 2000; Gasparre et al. 2007), and the dependence of stiffness on stress history and stress path (Atkinson et al, 1990; Hight & Higgins, 1995; Leroueil & Hight, 2003).

Atkinson (2000) advocated the use of simple analyses to assess in-situ ground stiffness for geotechnical design, where possible. This includes cases where movement is predominately one-directional, such as the settlement of a foundation or the horizontal movement at the top of a retaining wall. Empirical expressions for the secant shear modulus (G) of clays at a range of strain values include those developed from the interpretation of a database of tests on fine-grained soils (Darendeli 2001; Vardanega & Bolton 2013) and the interpretation of laboratory and field data using easily-obtained parameters (Atkinson 2000; O'Brien et al. 2023).

The construction of the UK High Speed 2 (HS2) railway between London and Birmingham has provided an opportunity to obtain monitoring data from geotechnical structures including tunnels, cuttings and embankments built on or through a range of geological strata from the Cretaceous, Jurassic and Triassic periods. Among these was a fully-instrumented trial embankment constructed on weathered clays and mudstones of the Jurassic Charmouth Mudstone Formation (Lias Group) at a site near Banbury, Oxfordshire. This is a case of predominately vertical loading and ground deformation that is suited to the simple back-analysis approach advocated by Atkinson (2000).

This paper aims to assess values of operational in-situ shear moduli for stiff fissured clays and weathered mudstones, at a range of pre-yield strains (<1%) relevant for the serviceability of geotechnical a structure. This is achieved by measuring and analysing the surface loading, pore water pressures and ground deformations during the construction of an instrumented trial embankment on weathered clays and mudstones, interpreted using site investigation data and in-situ geophysical measurements.

Materials

An instrumented trial embankment was constructed on stiff fissured clays and weathered mudstones of the Charmouth Mudstone Formation. The settlement of the trial embankment was monitored to inform the design and construction of earthworks located on mudstone outcrops in central England for the High Speed 2 railway (Munro, 2021). Construction of the trial embankment began on 7 November 2020 and was completed on 9 December 2020, when the embankment had reached a height of 8.2 m (Menteth, 2024). The embankment was constructed using fill material excavated from a deep (15 m) cutting excavation located directly to the south.

The site

The trial embankment was located within an outcrop of the Charmouth Mudstone Formation approximately 14 km to the north of Banbury (52°11’17”N, 1°20’25”W), Oxfordshire (Figure 2). The Charmouth Mudstone of the Lias Group was formed approximately 183-199 Myr ago and was formerly known as the Lower Lias Clay (Cox et al. 1999). The Charmouth Mudstone Formation was deposited in shallow seas and subsequently exposed to overconsolidation and weathering during glacial and periglacial conditions in the last 0.2 M years. The lithology of the formation is principally mudstone with thin limestone and sandstone bands; with weathered clay and some superficial deposits at shallower depth. Based on downhole geophysical logs, Hobbs et al. (2012) described the Charmouth Mudstone Formation in this region (the East Midlands Shelf) as 100-150 m thick, with a remarkably uniform internal stratigraphy across the region. At the site there is a gradational weathering profile from the ground surface (Briggs et al. 2022), resulting from glacial, periglacial and contemporary weathering in this location (Quaternary Province 4: Foster et al. 1999).

Seven cable percussion (to 10 mbgl) and rotary cored (>10 mbgl) boreholes were drilled in the ground beneath the embankment (ground level *c.* 122 mAOD) and rotary cored samples were taken for laboratory testing, as part of the HS2 ground investigation. The weathering profile was recorded according to BS 5930: 2015+A1:2020 ‘Approach 4’ for weak rocks. The borehole strata descriptions show weathered, firm to locally stiff fissured clay to 5 mbgl (117 mAOD) and weathered, stiff and very stiff fissured clay to 12 mbgl (110 mAOD). They show weathered, extremely weak fissured mudstone and unweathered extremely weak to very weak fissured mudstone below 12 mbgl (Figure 3). A 2m thick band of calcareous siltstone (i.e. limestone) was observed at approximately 18 mbgl (104 mAOD). Both the transition from clay to mudstone (~12 mbgl) and the calcareous siltstone (~18 mbgl) were visible in optical borehole images (not shown) obtained from beneath the centre of the embankment. Figure 3 shows the moisture content (%), plasticity index (%), specific volume, unit weight (kN/m^3) and undrained shear strength (kPa) from HS2 ground investigation data obtained within 0.25 km of the trial embankment. The moisture content reduced from approximately 25% near the surface (<2.5 mbgl) to approximately 20% at greater depth. The plasticity index reduced from approximately 35% at the near surface to approximately 30% at greater depth. The bulk unit weight increased with depth from 20.5 kN/m^3 to 21.5 kN/m^3. These are consistent with measurements in the Charmouth Mudstone Formation outcrop at this location (Briggs et al. 2022).

The trial embankment

Figure 2 shows a plan view of the trial embankment and the instrument locations. The embankment was constructed in stages between 7 November 2020 and 9 December 2020. It was approximately 150 m long and 95 m wide (at the base), with a crest width of 55 m and a slope angle of approximately 23°. The height of the embankment was measured by aerial drone surveys during construction and reached a final value of 8.2 m. Surface water runoff ponds were located to the north and the east of the site.

Instruments were installed in two groups, beneath the centre and the eastern edge of the crest of the embankment, prior to construction (Figure 2). Each group comprised an RST Instruments LPTPC09-V-LP vibrating wire total earth pressure cell at the ground surface to measure the load from the embankment, three RST Instruments VW2100 vibrating wire piezometers to measure pore water pressure and an RST Instruments EXINLINE-1100 vibrating wire inline extensometer to measure vertical displacement through the ground profile (Table 1). A Campbell Scientific CS106 barometer was installed adjacent to the trial embankment to record barometric pressure (hPa) at hourly intervals. The instruments were installed between August and October 2020 and were logged at hourly intervals from 5 November 2020 until the end of construction on 9 December 2020. Data logging continued beyond December 2020 to measure the long term consolidation behaviour of the trial embankment, to inform the design and construction of HS2 (Menteth, 2024; Briggs et al. 2024). Data measured after December 2020 extended beyond the immediate, undrained response of the ground to construction of the trial embankment and were therefore not considered in the analyses presented in this paper.

Total pressure cells

Total pressure cells (PC1 and PC2) were installed in shallow pits at the ground surface prior to embankment construction, protected by a 300 mm thick layer of sand. They were calibrated during installation by the application of known weights and remained responsive to changes in barometric pressure throughout the monitoring period. Figure 4 shows that the pressure applied to the ground surface increased as the embankment construction progressed in a series of stages, with greater pressure beneath the centre of the embankment (PC1) than beneath the edge of the embankment crest (PC2). The pressures measured at the two locations diverged as construction progressed, owing to their different positions relative to the edge of the embankment crest.

The total pressure cell measurements in Figure 4 were initially used to estimate the unit weight of the embankment fill at three stages of construction for which drone survey data of the height were available. The cell pressure measurements and the back-calculated unit weight of the fill were used to determine the embankment height for other stages of construction, for which no drone survey data were available.

All calculations accounted for both the position of the cells beneath the embankment in relation to the edge of the embankment crest and for the error inherent in the measurements, owing to the difference in stiffness between the cells and the medium into which they are inserted, quantified by means of a cell action factor F_{cell} (Peattie & Sparrow 1954; Clayton & Bica 1993). Weiler & Kulhawy (1982) identified fifteen extraneous influences on pressure cell measurements in soil including the cell dimensions, lateral stress rotation and the relative stiffness of the pressure cell and the soil. A cell action factor (F_{cell}) of 1.04 was adopted; that is, the measured pressure changes were assumed to be 4% greater than the true vertical stress changes beneath the embankment. This is consistent with cell action factors of 1.04 given by Tory & Sparrow (1967) and 1.04±0.03 given by Talesnick (2013) for an infinitely stiff sensor.

The elastic solution for pressures at the base of an embankment on elastic soil given by Perloff et al. (1967) was used to relate the embankment height and unit weight of the embankment fill to the pressure cell data (PC1 and PC2). The increase of embankment height (H) was estimated from the measurements at PC1, below the centre of the embankment, using:

$$H \approx \frac{\sigma_{PC1}}{\gamma_{emb} I_z F_{cell}}$$

Equation 1

where F_{cell} is the cell action factor, σ_{PC1} is the measured cell pressure at PC1 and γ_{emb} is the unit weight of the embankment fill. The influence factor (I_z) was derived from the chart presented by Perloff et al. (1967). The unit weight of the embankment fill was calculated using Equation 1 using the known embankment heights measured by drone surveys at PC1 on 23 November, 2 December and 9 December 2020. The resulting value of 22 kN/m^3 is similar to the bulk unit weight of the clay beneath the embankment (Figure 3).

The Perloff et al. (1967) influence factor beneath the edge of the crest of a long embankment with a 22.5° slope angle was approximated using linear functions (Appendix A), and used together with the pressure cell measurements at PC2, to obtain a second estimate of the height of the embankment (H):

$$H \approx \begin{cases} \dfrac{\sigma_{PC2}}{\gamma_{emb} F_{cell}} & when \ \dfrac{\sigma_{PC2}}{\sigma_{PC2,max}} \leq 0.49 \\ \dfrac{\sigma_{PC2}\sigma_{PC2,max}}{\gamma_{emb} F_{cell}(1.134\sigma_{PC2,max} - 0.275\sigma_{PC2})} & when \ \dfrac{\sigma_{PC2}}{\sigma_{PC2,max}} \geq 0.49 \end{cases}$$

Equation 2

where F_{cell} is the cell factor, σ_{PC2} is the measured cell pressure at PC2, $\sigma_{PC2,max}$ is the measured cell pressure at PC2 when the embankment is at maximum height and γ_{emb} is the unit weight of the embankment. Perloff et al. (1967) assumed a Poisson's ratio of 0.3 and did not consider any other values, but according to Poulos and Davis (1974) the effect of this parameter is small for embankments, like this one, that are relatively wide (width L / height H > 5). Figure 5 shows the calculated increases in embankment height with time using the measurements at PC1 and PC2, the measurements of actual embankment height at PC1 at three loading stages on 23 November, 2 December and 9 December 2020, and the eight loading stages selected for the shear stiffness analyses.

Piezometers

The vibrating wire piezometers (Table 1) installed beneath the centre of the embankment (PIEZO1) and the edge of the embankment crest (PIEZO2) were submerged in de-aired water before being lowered into the borehole (facing upwards). They were grouted in place using a water-cement-bentonite grout (2.0 : 1.0 : 0.3 by weight) to maintain hydraulic connectivity with the soil. The piezometers showed a hydrostatic pore water pressure profile below a water table approximately 0.8-1 mbgl prior to embankment construction. The measurements from the shallower (≤ 20 mbgl) piezometers beneath the centre of the embankment showed that pore water pressures rapidly increased in response to each loading stage (Briggs et al. 2024). This was followed by a slight reduction in pore water pressure (indicating a little drainage) beneath the edge of the embankment crest between each loading stage, but this was small (1-2 kPa) relative to the applied changes in total stress (up to 190 kPa). The piezometers at greater depth (> 20 mbgl) showed a smaller response to the embankment loading, consistent with the attenuation of vertical stress with depth.

Extensometers

The vibrating wire in-line extensometers (Table 1) beneath the centre of the embankment (EXT1) and beneath the edge of the embankment crest (EXT2) were installed to depths of 60 mbgl and 50 mbgl respectively. Each extensometer included six Borros hydraulic anchors installed at specified depths. These were connected to six displacement transducers in series, separated by stainless steel rods within a PVC sheath. During installation the anchors were hydraulically activated in ascending order from the base of the borehole, then grouted in place using a water-cement-bentonite grout (6.6 : 1.0 : 0.4 by weight). Table 2 shows the displacements of the extensometer anchors at various depths, relative to the deepest anchor at the base of the extensometer.

Table 2 shows that during embankment construction there was negligible displacement in EXT2 between the anchor at 35 mbgl and the base anchor 50 mbgl. The displacement of the anchors at shallower depth (0, 2.5, 7.5, 15 & 25 mbgl) increased with each embankment loading stage. At EXT1, the measurements between the anchor at 40 mbgl and the base anchor at 60 mbgl showed some noise. They increased gradually to 1 mm at Stage 5 (27 November 2020), then reduced. This suggests that some dislocation of the base anchor may have occurred during loading stage 5; the potential for error was mitigated by using the displacement between adjacent extensometer anchors, rather than displacements relative to the base anchor, in calculations.

Figure 6 shows the relative displacement (δ_{Layer}) between adjacent extensometer anchors in each borehole during construction of the trial embankment. The relative displacements of the shallowest anchor pairs between 0 mbgl and 5 mbgl (EXT1) and between 0 mbgl and 2.5 mbgl (EXT2) were an order of magnitude greater than for the deeper anchors. They are therefore omitted from Figure 6 for clarity, but are recorded in Table 3. The measurements show increasing relative displacements between the pairs of adjacent anchors down to at 40 mbgl at EXT1 (Figure 6(a)), and down to 35 mbgl at EXT2 (Figure 6(b)). Note that the soil layers shown in Figure 6 are not of equal thickness.

In-situ testing

Downhole seismic tests were undertaken in four boreholes by a specialist contractor for the HS2 ground investigation. Optical image logs were obtained from one borehole (DHGEO_3) using a precision-machined prism and CCD camera. The boreholes were located approximately 250 m to the south of the trial embankment, at elevations between 134 and 136 mAOD. The borehole records showed weathered, stiff to very stiff fissured clay to 13 mbgl (113 mAOD), with mudstone below. The calcareous siltstone (i.e. limestone) was located within the mudstone at approximately 32 mbgl (102 mAOD).

P-wave and S-wave seismic velocities were measured at 1 m intervals of depth within plastic-lined boreholes, to 63 mbgl. The S-waves were generated by a sledgehammer striking the end of a timber sleeper at the ground surface. The P-waves were generated by vertically striking an acrylic plate at the ground surface with a sledgehammer. The seismic waves were detected by a BGK-7 multi element geophone having one vertical and six horizontal sensors, pneumatically clamped within the borehole at each successive test depth.

Figure 7 shows a linearly-increasing shear wave velocity (V_s) with increasing depth within all four boreholes, to approximately 20 mbgl. The measurements in the mudstone at greater depth (> 20 mbgl) vary between individual boreholes. The borehole records showed no change in the visual appearance of the mudstone weathering profile that might explain the increased variation in geophysical measurements below 20 mbgl. Similarly, no change was visible in the optical images from DHGEO_3 (not shown). However, this depth is consistent with the transition between the weathered (Class Ba) and the unweathered (Class A) material across the Charmouth Mudstone Formation outcrop at the site location (Briggs et al. 2022). The measured compression wave velocities (V_p) shown in Figure 7 were less than for water (approx. 1500 m/s) at depths to 40 mbgl and hence of limited use. This is typical of soft rocks (Clayton 2011; Poulos 2022).

The downhole geophysical measurements (Figure 7) and sample unit weight measurements (Figure 3) were used to produce a profile of shear modulus at very small strain (G_0) for the weathered clay and mudstone layers (up to 20 mbgl) using the relationship (Zisman 1933; Atkinson 2000; Poulos 2022):

$$G_0 = \rho {V_s}^2 = \frac{\gamma_b}{g} {V_s}^2$$

Equation 3

where ρ is the bulk density (kg/m^3), γ_b is the bulk unit weight (kN/m^3), g is the acceleration of the Earth's gravity (m/s^2) and V_s is the shear wave velocity (m/s). The shear modulus at very small strain (G_0) from the downhole geophysical measurements was considered as the maximum (G_{max}).

For comparison, a profile of maximum shear modulus (G_{max}) with depth was determined using the unit weight and specific volume of the samples (Figure 3) as inputs for the Vardanega & Bolton (2013) equation for fine-grained soils tested in laboratory conditions:

$$\frac{G_{max}}{p'_r} = \frac{B}{(v)^{2.4}} \left(\frac{p'}{p'_r}\right)^{0.5}$$

Equation 4

where p' is the mean effective stress, p'_r is a reference stress (taken as 1 kPa) and v is the specific volume of the triaxial samples obtained close to the trial embankment (Figure 3). A soil structure coefficient , B, was selected for a typical fine-grained soil (B = 20,000) and for an overconsolidated aged clay (B = 50,000), as described in Vardanega & Bolton (2013). Figure 8 shows an increasing profile of G_{max} with depth at the site. This is in close agreement with the Vardanega & Bolton (2013) profile for typical fine-grained soils (B= 20,000) to 8 mbgl. There is greater scatter in the downhole geophysical measurements below 8 mbgl. Therefore, separate linear (regression) fits for G_{max} were derived for the weathered clay (0-8 mbgl) and the less-weathered clay and mudstone below (> 8 mbgl). The value of G_{max} at greater depth in the less-weathered clay and mudstone layers (> 11 mbgl) lies closer to the Vardanega & Bolton (2013) profile for overconsolidated aged clay (B= 50,000).

Methods

The essence of the approach was to use the embankment loading and extensometer data at known construction stages to calculate the in-situ shear modulus profile of the Charmouth Mudstone Formation beneath the embankment. Together with the downhole geophysical measurements, these were used to determine the shear modulus reduction with strain curve. The method can be summarised as:

1. Data from the pressure cells and aerial drone surveys of embankment height were used to obtain the magnitude and distribution of loading at the ground surface at selected stages (loading stages) during construction of the embankment.

2. Relative displacements measured between adjacent extensometer anchors were used to determine the average vertical strains within selected layers below the embankment.

3. The vertical strains, together with the surface loading and elasticity equations, were used to determine the representative stresses and strains below the embankment on a layer-by-layer basis at selected loading stages.

4. Corresponding shear stresses and shear strains were used to calculate the operational secant shear modulus and secant shear strain for each layer and loading stage.

6. A profile of maximum shear modulus against depth was obtained from down-hole seismic tests.

7. Finally, plots of normalised secant shear modulus against shear strain were obtained for each layer and loading stage.

The shear modulus and shear modulus reduction curve were calculated for layers within the weathered clay and weathered mudstone ground profile, to 20 mbgl. They were not calculated for the unweathered mudstone at greater depth (>20 mbgl), because the measured displacements were very small (<2 mm) below this depth (Table 2). The analyses assumed an immediate, undrained ground response to the surface loading. The piezometers did show some drainage beneath the edge of the embankment crest at shallower depth (up to 10 mbgl) between the loading stages (Briggs et al. 2024), but the small (1-2 kPa) pore water pressure change relative to the applied loading (20-170 kPa) justifies the assumption of substantially undrained conditions.

Calculation of stress increases associated with embankment construction

Construction of the trial embankment increased the total stresses in the underlying ground. The increases in vertical, horizontal and shear stress (σ_z, σ_x and τ_{zx} respectively) were calculated for each layer (between adjacent extensometer anchors) in each ground profile (beneath the centre and the edge of the embankment crest) at each selected stage of construction (Figure 5). The changes in stresses were calculated using the analytical equations for stress increments in an elastic half-space under vertical loading and plane-strain conditions, derived by Gray (1936) and summarised in Poulos & Davis (1974). These equations assume a linear elastic, homogeneous, isotropic material and can be superimposed to derive solutions for geometrically more complicated loading scenarios, such as a different location beneath an embankment. The equations are:

$$\Delta\sigma_z = \frac{P}{\pi}\left[\beta + \frac{x\alpha}{a} - \frac{z}{R_2^2}(x-b)\right]$$

Equation 5

$$\Delta\sigma_x = \frac{P}{\pi}\left[\beta + \frac{x\alpha}{a} - \frac{z}{R_2^2}(x-b) + \frac{2z}{a}\ln\frac{R_1}{R_0}\right]$$

Equation 6

$$\Delta\tau_{xz} = -\frac{P}{\pi}\left[\frac{z\alpha}{a} - \frac{z^2}{R_2^2}\right]$$

Equation 7

where $\Delta\sigma_z$ is the change in vertical stress, $\Delta\sigma_x$ is the change in horizontal stress (in the vertical cross-sectional plane), $\Delta\tau_{xz}$ is the change in shear stress, *P* is the surface load, *x* is the horizontal location, *z* is the vertical location (i.e. depth) and the geometry parameters are defined in Figure 9. The surface load (*P*) at each load stage was equal to the unit weight of the embankment fill (γ_{emb} = 22 kN/m^3) multiplied by the height of the embankment, *H* (as shown in Figure 5 and Table 2). The embankment width geometry parameter, *b*, was half the embankment width. The slope width parameter, *a*, varied as the embankment height increased (for a slope angle of 22.5^o).

Changes in stress were calculated at the top ($\Delta\sigma_{Top}$), midpoint ($\Delta\sigma_{Mid}$) and base ($\Delta\sigma_{Base}$) of the layers beneath the centre of the embankment (EXT1) and beneath the edge of the embankment crest (EXT2). These were used to derive the weighted average change in stress in each layer ($\Delta\sigma_{LayerAve}$) using Simpson's rule (Atkinson 1989):

$$\Delta\sigma_{LayerAve} = \frac{1}{6}\left[\Delta\sigma_{Top} + 4\Delta\sigma_{Mid} + \Delta\sigma_{Base}\right]$$

Equation 8

The weighted average changes in vertical stress ($\Delta\sigma_{zLayerAve,Stage}$), horizontal stress ($\Delta\sigma_{xLayerAve,Stage}$) and shear stress ($\Delta\tau_{xzLayerAve,Stage}$) were calculated for each layer, for each embankment loading stage.

Calculation of vertical strains

The average vertical strains were calculated for each stage of embankment construction and for each layer ($\varepsilon_{zLayer,Stage}$), from the relative displacement between adjacent pairs of extensometer anchors, $\delta_{zLayer,Stage}$ (Figure 6) and the initial layer thickness, Z_{0Layer} (that is, the initial extensometer anchor spacing):

$$\varepsilon_{zLayer,Stage} = \frac{\delta_{zLayer,Stage}}{Z_{0Layer}}$$

Equation 9

Vertical strains were calculated for three layers beneath the centre of the embankment at EXT1 (0 to 5 mbgl, 5 to 10 mbgl and 10 to 20 mbgl) and three layers beneath the edge of the embankment crest at EXT2 (0 to 2.5 mbgl, 2.5 to 7.5 mbgl and 7.5 to 15 mbgl). These are the layers for which the relative displacement between adjacent extensometer anchors was greater than 1.1 mm (Table 3). The layers at greater depths (>20 mbgl), with relative displacements below this threshold, were excluded from the analyses. The depth threshold of 20 mbgl corresponded with the transition from a uniform to a more scattered shear wave velocity profile in the nearby downhole seismic tests (Figure 7), and with the transition from weathered (Class Ba) to unweathered (Class A) mudstone observed across the Charmouth Mudstone Formation outcrop locally (Briggs et al. 2022).

Calculation of the in-situ shear modulus, shear strain and normalised shear modulus

The operational secant shear modulus for each layer and embankment loading stage ($G_{Layer,Stage}$) was calculated using the stress-strain relationship (rearranged from Equation 1.36c in Poulos & Davis 1974):

$$G_{Layer,Stage} = \frac{1}{2\varepsilon_{zLayer,Stage}}\left[\left(\Delta\sigma_{zLayerAve,Stage}(1-\upsilon_u)\right) - \left(\upsilon_u\Delta\sigma_{xLayerAve,Stage}\right)\right]$$

Equation 10

where v_u is the undrained Poisson's ratio (taken as 0.5). The plane-strain shear stress and shear strain invariants were calculated for each layer and embankment loading stage to find the maximum shear strains, for comparison with the Vardanega & Bolton (2013) laboratory test results. The change in the plane-strain shear stress invariant, i.e. the radius of the Mohr circle in the cross-sectional plane, was calculated using:

$$\Delta\tau_{Layer\ Ave,Stage} = \sqrt{\frac{1}{4}\left(\Delta\sigma_{zLayer\ Ave,Stage} - \Delta\sigma_{xLayer\ Ave,Stage}\right)^2 + \Delta\tau^2{}_{xzLayer\ Ave,Stage}}$$

Equation 11

The in-situ, plane-strain shear strain invariant ($\gamma_{Layer,Stage}$) was calculated for each layer and for each stage of embankment construction as:

$$\gamma_{Layer,Stage} = \frac{\Delta\tau_{LayerAve,Stage}}{G_{Layer,Stage}}$$

Equation 12

Finally, the secant shear modulus for each layer and embankment loading stage ($G_{Layer,Stage}$) was normalised by the maximum shear modulus (G_{max}) at the midpoint of each layer. Values of G_{max} were derived from linear regression fits (depth vs G_{max}) to the downhole geophysical measurements for 0-8 mbgl and 9-20 mbgl, as shown in Figure 8.

For comparison, a normalised secant shear modulus reduction with strain curve was also calculated using the Vardanega & Bolton (2013) empirical relationship for fine-grained soils. This includes an adjustment (referred to as a 'static adjustment') for shear strain rates in static laboratory tests:

$$\frac{G}{G_{max}} = \frac{1}{1 + \left(\frac{\gamma}{\gamma_{ref}}\right)^{\alpha}}$$

Equation 13

and

$$\gamma_{ref} = J\left(\frac{I_p}{1000}\right)$$

Equation 14

where γ is the shear strain, γ_{ref} is the reference shear strain at $0.5G_{max}$, α is a fitting parameter (set equal to 0.736, as used in Vardanega & Bolton (2013)), I_p is the plasticity index (expressed as a fraction rather than a percentage) and J is a regression coefficient relating I_p and γ_{ref} (where J = 2.2 in Vardanega & Bolton (2013)). Curves were calculated for plasticity indices (I_p) of 5% to 35%.

Results and discussion

Figure 10 shows the resulting graphs of normalised secant shear modulus against shear strain for six layers beneath the embankment, and eight loading stages. For comparison, empirical curves defined by the Vardanega & Bolton (2013) empirical equation (Equation 13) are shown for plasticity indices ranging from 5% to 35%.

Figure 10 shows the expected behaviour of decreasing normalised secant shear modulus with increasing shear strain within all the layers beneath the embankment. The measurements from the shallowest layers (0-5 mbgl) are close to zero (less than 0.015) at ≈1% strain, and are located below the Vardanega & Bolton (2013) empirical curves. The results from the soil layers between 2.5 mbgl and 7.5 mbgl are close to the Vardanega & Bolton (2013) curve for a plasticity index (I_p) of 15%. These layers are the weathered, stiff and very stiff fissured clays with a plasticity index (I_p) of 26 - 31% (Figure 3). The results from the stiffer (Figure 8), less-weathered clays and weathered mudstones between 5 mbgl and 20 mbgl (I_p ≈28%) are close to the Vardanega & Bolton (2013) curve for a plasticity index (I_p) of 5%. Therefore, the measurements from beneath the trial embankment show decreasing values of reference strain (γ_{ref}) with increasing depth (and a slight decrease in plasticity; Figure 3). They fit the general reduction trend of the Vardanega & Bolton (2013) curves, as determined by parameter α, but show lower values of the reference strain (γ_{ref}). The measurements correspond with Vardanega & Bolton (2013) curves for lower values of the plasticity index compared to index test data for the site (Figure 3). It should be noted that the data in Figure 10 assume undrained conditions and that no volume change takes place (i.e. ν_u = 0.5). However, due to the high stiffness of the materials, some undrained volume change may occur due to the compressibility of the water or dissolved air (Briggs et al. 2024). The implications of this are explored in Appendix B.

Figure 11 shows the inferred vertical stress-strain plots for the six layers within the ground profile beneath the trial embankment. Figure 11a shows that the vertical strains were approaching values associated with yield (>1%) in the shallowest layers (up to 5 mbgl). While the secant modulus decreased with vertical strain, the tangent modulus (given by the slope of the graph) increased. This may be a result of the drainage and consolidation in these shallowest layers, particularly beneath the edge of the embankment crest. Figure 11b shows that the vertical strains in the layers >5 mbgl were in the medium strain range (up to 0.08%). These layers showed decreasing secant and tangent moduli with vertical strain. Figure 12 shows the operational secant shear modulus (G) and shear strain (γ) of six layers within the ground profile beneath the centre and the edge of the crest of the embankment. The deeper clay and mudstone layers (grey symbols) had the highest shear modulus due to their greater in-situ stress and lower void ratio, in agreement with the geophysical measurements (Figure 8). This reduced rapidly with shear strain, but reference to Figure 10 shows that this was proportional to G_{max}. Figure 12 shows that the reduction of shear modulus with shear strain in the shallower clay layers (black symbols) was more comparable to the mean curve for fine-grained soils, as described in the Vardanega & Bolton (2013) database (where I_p= 39%, p'=209 kPa, G_{max} = 68 MPa).

The shear modulus obtained from the downhole geophysical measurements (Figure 8) and the shear stress-strain relationships obtained from the back-analyses (Figure 10 and Figure 12) show the influence of weathering on the in-situ ground profile at the site. The weathered clay (0-8 mbgl) exhibited a maximum shear modulus (G_{max}) profile comparable with those measured in other fine-grained materials, as demonstrated by the close fit to the Vardanega & Bolton (2013) equations. However, the maximum shear modulus (G_{max}) profile of the less-weathered clay and weathered mudstone (>8 mbgl) was larger and more variable than for the weathered clay. It was larger than values derived from the Vardanega & Bolton (2013) equation for typical fine-grained soils (i.e. B = 20,000), and was closer to those for overconsolidated aged clays (i.e. B = 50,000). The shear modulus (G) of the deeper layers (7.5 to 15 mbgl and 10 to 20 mbgl) reduced more rapidly with shear strain (γ) than in the overlying layers. These less weathered, and hence more structured, clays and mudstones were initially stiffer than the shallower, more weathered clays. However, the normalised shear modulus (G/G_{max}) in all layers reduced at a rate that was comparable to the Vardanega & Bolton (2013) equation, over the range of medium strains relevant to geotechnical structures.

At intermediate depths (approximately 8-12 mbgl), the results showed a maximum shear modulus profile that was between that of the weathered clay and the mudstone. This transition compares to those in the gradational weathering profile in the wider Charmouth Mudstone Formation (Briggs et al. 2022), as shown by the results of visual inspection, soil classification tests and undrained unconsolidated (UU) triaxial compression tests.

The Poulos & Davis (1974) elasticity equations enabled back-analyses for the simple case of predominately vertical loading and ground deformation at the trial embankment. It includes assumptions of undrained loading, linear elasticity and isotropic, homogenous ground stiffness. The assumption of undrained behaviour in the clay and mudstone is justified by the relatively short duration of the embankment trial construction (32 days) and the short (1-7 day) intervals between the embankment loading stages.

The elastic half space model assumes a constant shear modulus throughout the ground profile, but the results showed that the shear modulus increased linearly with depth. However, it is well-known that vertical stress changes beneath loaded areas are insensitive to nonlinear stress-strain behaviour, stiffness anisotropy and increasing stiffness with depth (Burland et al. 1977). This was confirmed by supplementary finite element analyses in Sigma/w (GEO-SLOPE International Ltd, 2013) assuming a linear elastic material (not reported in this paper). This showed that the calculated changes in vertical total stress were not sensitive to the use of a constant or a linearly increasing shear modulus profile. Further, these analyses showed that, for the geometry of the trial embankment, the calculated changes in horizontal total stress were also insensitive (<1% difference) to a stiffness increasing with depth, and to a stiffness anisotropy in the range indicated by laboratory and in-situ measurements in clays and mudstones of 1.5 to 2 horizontal:vertical (Mitchell & Soga 2005; Clayton 2011). Burland (2012) has also shown that stiffness anisotropy has a limited influence on the change in vertical stresses beneath a uniform surface load, such as an embankment.

Conclusions

Instrumentation installed beneath a trial embankment was used to measure the settlement of the underlying foundation of weathered clays and weathered mudstones, in response to the staged construction of an 8.2 m high, clay fill embankment. The measurements showed the vertical deformation of the foundation in response to the applied surface load. Complementary, in-situ measurements of shear modulus using downhole geophysical methods showed that the foundation maximum shear modulus increased with depth up to 20 mbgl. The calculated distributions of stress increase and measured strains were used to determine the secant shear modulus of the foundation strata at a range of depths and shear strains. This led to the following conclusions.

1. The maximum shear modulus (G_{max}) of the Charmouth Mudstone Formation increases with depth and is influenced by the in-situ weathering profile. Measurements within the weathered, stiff and very stiff fissured clays compare well with the Vardanega & Bolton (2013) empirical correlation for typical fine-grained soils (i.e. B = 20,000), up to a depth of 8 mbgl. Below this depth, the maximum shear modulus (G_{max}) is 50-100 MPa greater than for typical fine-grained soils. At depth (> 11 mbgl) the Vardanega & Bolton (2013) equation for overconsolidated aged clay (i.e. B = 50,000) is more comparable to the maximum shear modulus (G_{max}). The measured shear modulus profile aligns with the transitions from weathered clay (<13 mbgl) to weathered mudstone (≈13-20 mbgl) and unweathered mudstone (>20 mbgl) shown in the corresponding borehole records. These compare with the gradational weathering profile in the wider Charmouth Mudstone Formation outcrop at the site location (Briggs et al. 2022).

2. The normalised secant shear modulus (G/G_{max}) of weathered clays and mudstones were determined using extensometers, a known surface load and complementary geophysical measurements of the maximum shear modulus (G_{max}). Extensometer anchors installed at multiple depths beneath an increasing surface load, such as an embankment under construction, allow the shear modulus of the ground to be calculated for multiple stress increments and for a range of strain values. Critically, it is possible to obtain in-situ shear modulus measurements at a range of strains that are relevant for the serviceability design of geotechnical structures (<1% strain). These are not routinely measured in laboratory triaxial tests or in materials that are difficult to sample, such as stiff clays and weak rocks.

3. The Vardanega & Bolton (2013) empirical equation for normalised secant shear modulus reduction with strain compared with in-situ measurements from the weathered clays and mudstones beneath the trial embankment (0 mbgl to 20 mbgl). The in-situ measurements from the shallower, more plastic clay layers showed larger values of reference strain (γ_{ref}) than the deeper layers of less-weathered, more structured and less plastic clay and mudstone. This is in agreement with the Vardanega & Bolton (2013) empirical correlations for fine-grained soils of varying plasticity index. However, the plasticity indices of the Vardanega & Bolton (2013) curves that fit the in-situ measurements (I_p of 5% - 15%) are much lower than the measured plasticity indices of the clays and mudstones beneath the trial embankment (I_p of 26% - 31%). Therefore, the values for the reference strain (γ_{ref}) that compare to the in-situ measurements are lower than would be predicted by the empirical equations.

Acknowledgements

This work was supported by the Royal Academy of Engineering and HS2 Ltd under the Senior Research Fellowship scheme (RCSRF1920\10\65) and the ACHILLES Engineering and Physical Sciences Research Council (EPSRC) programme grant led by Newcastle University (EP/R034575/1). The data were provided by HS2 Ltd. Thank you to N. Bicocchi, D. Fornelli and A. Ridley at Geo-Observations Ltd, H. Wood at COWI and to R. Bichener, D. Richardson, G. Barker and G. Hemmings at EKFB for invaluable discussions and assistance with obtaining data and materials. Thank you to A.S. O'Brien for helpful suggestions during the interpretation. The first author would like to thank the late L. Barbour (University of Saskatchewan) for his support and mentoring during the early stages of this investigation.

Competing interests

Competing interests: The authors declare there are no competing interests.

Data availability

The data presented in this paper are available online via the University of Bath institutional repository (Briggs, 2024a) and may be accessed at https://doi.org/10.15125/BATH-01353.

References

Atkinson, K. E. 1989. *An Introduction to Numerical Analysis* (2nd ed.). John Wiley & Sons. ISBN 0-471-50023-2.

Atkinson, J.H., Richardson, D. and Stallebrass, S.E., 1990. Effect of recent stress history on the stiffness of overconsolidated soil. *Géotechnique*, 40(4), pp.531-540.

Atkinson, J.H., 2000. Non-linear soil stiffness in routine design. *Géotechnique*, 50(5), pp.487-508.

Briggs, K.M., Blackmore, L., Svalova, A., Loveridge, F.A., Glendinning, S., Powrie, W., Butler, S. and Sartain, N., 2022. The influence of weathering on index properties and undrained shear strength for the Charmouth Mudstone Formation of the Lias Group at a site near Banbury, Oxfordshire, UK. *Quarterly Journal of Engineering Geology and Hydrogeology*, 55 (3). https://doi.org/10.1144/qjegh2021-066

Briggs, K.M., Trinidad González, Y., Meijer, G.J., Ridley, A., Powrie, W., Butler, S. and Sartain, N., 2024. The influence of earthworks construction on pore water pressures in clays and mudstones of the Lias Group. *Quarterly Journal of Engineering Geology and Hydrogeology, 57 (4).* https://doi.org/10.1144/qjegh2024-036

Briggs, K., 2024a. *Dataset of measurements at an instrumented embankment trial on an outcrop of the Charmouth Mudstone Formation (Lias Group) in central England*. Bath: University of Bath Research Data Archive. https://doi.org/10.15125/BATH-01353

British Standards Institution 2004. *BS EN 1997-1:2004 Eurocode 7: Geotechnical design. General rules*. BSI, London, UK.

British Standards Institution 2017. *BS EN ISO/IEC 17025:2017. General requirements for the competence of testing and calibration laboratories.* BSI, London, UK.

British Standards Institution 2020. *BS 5930:2015+A1:2020. Code of Practice for Ground Investigations*. BSI, London.

Burland, J.B., Broms, B.B. and De Mello, V.F., 1978. Behaviour of foundations and structures. State of the art review. *9th International Conference on Soil Mechanics Foundation Engineering*, 2, 495-546.

Burland, J. B. 1989. Small is beautiful: the stiffness of soils at small strains. Ninth Laurits Bjerrum Lecture. *Canadian Geotechnical Journal*, 26, No. 4, 499-516.

Burland, J.B. 2012. Chapter 19 Settlement and stress distributions. *In ICE manual of geotechnical engineering* (pp. 207-220). Thomas Telford Ltd.

Clayton, C.R.I. & Bica, A.V.D. 1993. The design of diaphragm-type boundary total stress cells. *Géotechnique*, 43(4), pp.523-535.

Clayton, C.R.I., 2011. Stiffness at small strain: research and practice. *Géotechnique*, 61(1), pp.5-37.

Cox, B.M., Sumbler, M.G. and Ivimey-Cook, H.C. 1999. *A Formational Framework for the Lower Jurassic of England and Wales (Onshore Area)*. British Geological Survey Research Report RR/99/01. British Geological Survey, Keyworth, Nottingham, UK.

Darendeli, M.B., 2001. *Development of a new family of normalized modulus reduction and material damping curves*. The University of Texas at Austin.

Foster, S.S.D., Morigi, A.N. and Browne, M.A.E. 1999*. Quaternary Geology – Towards Meeting User Requirements*. British Geological Survey, Keyworth, Nottingham, UK.

Gasparre, A., Nishimura, S., Minh, N.A., Coop, M.R. and Jardine, R.J. 2007. The stiffness of natural London Clay. In *Stiff Sedimentary Clays: Genesis and Engineering Behaviour: Géotechnique Symposium in Print 2007* , (57), 1. Thomas Telford Ltd.

Geomatrix Earth Science, 2023. *BGK Data Sheet*. Accessed 2023 at www.geomatrix.co.uk/land-products/seismic/bgk/.

GEO-SLOPE International Ltd (2013). Stress-deformation modelling with Sigma/w, an engineering methodology. July 2013 edition.

Gibson, R.E. and Sills, G.C., 1971. Some results concerning the plane deformation of a non-homogeneous elastic half-space. In *Proceedings of the Roscoe Memorial Symposium* (pp. 564-572).

Gray, H., 1936. Stress distribution in elastic solids. In *Proceedings International Conference on Soil Mechanics and Foundation Engineering* (Vol. 2, pp. 157-168).

Hight, D. W. & Higgins, K. G. 1995. An approach to the prediction of ground movements in engineering practice: background and application. *Proceedings International Symposium on Pre-failure Deformations of Geomaterials, IS-Hokkaido* 2, 909-945.

Hight, D.W., Gasparre, A., Nishimura, S., Jardine, R.J., Coop, M.R. and Minh, N., 2007. Characteristics of the London Clay from the Terminal 5 site at Heathrow Airport. In *Stiff Sedimentary Clays: Genesis and Engineering Behaviour: Géotechnique Symposium in Print 2007*, (57), 1 Thomas Telford Ltd.

Hobbs, P.R.N., Entwisle, D.C., Northmore, K.J., Sumbler, M.G., Jones, L.D., Kemp, S., Self, S., Barron, M. & Meakin, J.L. 2012. *Engineering Geology of British Rocks and Soils: Lias Group*. British Geological Survey Internal Report OR/12/032. British Geological Survey, Keyworth, Nottingham, UK

Horton, A. & Poole, E.G. 1977. The lithostratigraphy of three geophysical marker horizons in the Lower Lias of Oxfordshire. *Bulletin of the Geological Survey of Great Britain*, (62).

Ishihara, K. (1996). Soil behaviour in earthquake geotechnics. In *Oxford Engineering Science Series 46*, UK: Oxford, 350pp. Oxford University Press. ISBN: 0-19-856224-1

Jardine, R.J., Symes, M.J. and Burland, J.B., 1984. The measurement of soil stiffness in the triaxial apparatus. *Géotechnique*, 34(3), pp.323-340.

Jardine, R. J., Potts, D. M., Fourie, A. B. & Burland, J. B. 1986. Studies of the influence of nonlinear stress–strain characteristics in soil–structure interaction. *Géotechnique*, 36, No. 3, 377–397, doi: 10.1680/geot.1986.36.3.377.

Kelly, R.M.G., Bergamo, P., Hughes, D.A., Donohue, S., Barbour, S.L. and Lynch, K., 2018. A comparison of small strain stiffness in till as measured by seismic refraction and barometric loading response. *Quarterly Journal of Engineering Geology and Hydrogeology*, 51(4), pp.493-502.

Le, T., Standing, J. and Potts, D., 2023. Reassessing variations in the small-strain stiffness of London Clay. *Géotechnique*, pp.1-15.

Leroueil S. and Hight D.W. 2003. Behaviour and properties of natural soils and soft rocks. In *Characterisation and Engineering Properties of Natural Soils* (Tan TS, Phoon KK, Hight DWand Leroueil S (eds)). A.A. Balkema, Rotterdam, the Netherlands, vol. 1, pp. 29–254.

Lings M.L., Pennington D.S. and Nash D.F.T. 2000. Anisotropic stiffness parameters and their measurement in a stiff natural clay. *Géotechnique* 50(2): 109–125, https://doi.org/10.1680/geot.2000.50.2.109.

Mair, R.J., 1993. Unwin Memorial Lecture 1992: developments in geotechnical engineering research: application to tunnels and deep excavations. In *Proceedings of the Institution of Civil Engineers-Civil Engineering* (Vol. 97, No. 1).

Menkiti, C.O., Long, M., Kovacevic, N., Edmonds, H.E., Milligan, G.W.E. and Potts, D.M., 2004. Trial excavation for cut and cover tunnel construction in glacial till-a case study from Dublin. In *Advances in geotechnical engineering: The Skempton conference: Proceedings of a three day conference on advances in geotechnical engineering, organised by the Institution of Civil Engineers and held at the Royal Geographical Society, London, UK, on 29–31 March 2004* (pp. 1090-1104). Thomas Telford Publishing.

Menteth, T, 2024. 'Earthworks experiments', *Ground Engineering*, January 2024, p. 14-16.

Munro, A. 2021. HS2 railway, UK – why the country needs it. *Proceedings of the Institution of Civil Engineers – Transport*, 174, 3–11, https://doi.org/10.1680/ jtran.18.00040

Ng, C., Bolton, M. and Dasari, G., 1995. The small strain stiffness of a carbonate stiff clay. *Soils and foundations*, 35(4), pp.109-114.

Ng, C.W., Simpson, B., Lings, M.L. and Nash, D.F., 1998. Numerical analysis of a multipropped excavation in stiff clay. *Canadian Geotechnical Journal*, 35(1), pp.115-130.

O'Brien, A.S., Ho, X. and Tan, R., 2023. Non-linear stiffness characterisation–a practical framework. *Proceedings of the Institution of Civil Engineers-Geotechnical Engineering*, pp.1-15.

Peattie, K.R. and Sparrow, R.W., 1954. The fundamental action of earth pressure cells. *Journal of the Mechanics and Physics of Solids*, 2(3), pp.141-155.

Perloff, W.H., Baladi, G.Y., and Harr, M.E. 1967. Stress distribution within and under long elastic embankments. Highway Research Record 181, Washington, D.C., pp. 12–41.

Poulos, H.G., & Davis, E.H., 1974. *Elastic solutions for soil and rock mechanics*, John Wiley & Sons New York. ISBN 0-471-69565-3.

Poulos, H.G., 2022. Use of shear wave velocity for foundation design. *Geotechnical and Geological Engineering*, 40(4), pp.1921-1938.

Smith, L., Elwood, D., Barbour, S.L. and Hendry, M.J., 2018. Profiling the in situ compressibility of cretaceous shale using grouted-in piezometers and laboratory testing. *Geomechanics for Energy and the Environment*, 14, pp.29-37.

Talesnick, M., 2013. Measuring soil pressure within a soil mass. *Canadian Geotechnical Journal*, 50(7), pp.716-722.

Tatsuoka, F., Hayano, K. and Koseki, J., 2003. Strength and deformation characteristics of sedimentary soft rock in the Tokyo metropolitan area. *Proc. of Characterization and Engineering Properties of Natural Soils, Swets and Zeitlinger*, pp.1461-1525.

Tory, A.C., and Sparrow, R.W. 1967. The influence of diaphragm flexibility on the performance of an earth pressure cell. *Journal of Scientific Instruments*, 44: 781–785. doi:10.1088/0950- 671/44/9/333.

Vardanega, P.J. and Bolton, M.D., 2013. Stiffness of clays and silts: Normalizing shear modulus and shear strain. *Journal of Geotechnical and Geoenvironmental Engineering*, 139(9), pp.1575-1589.

Weiler Jr, W.A. and Kulhawy, F.H., 1982. Factors affecting stress cell measurements in soil. *Journal of the Geotechnical Engineering Division*, 108(12), pp.1529-1548.

Zisman, W.A., 1933. Young's modulus and Poisson's ratio with reference to geophysical applications. *Proceedings of the National Academy of Sciences*, 19(7), pp.653-665.

Figures and Tables

Figure 1: A shear stiffness reduction curve showing the typical strain range for geotechnical structures, analysis types and the approximate range of different measurement methods. Redrawn from Mair (1993), Ishihara (1996), Atkinson (2000), Clayton (2011) and O'Brien et al. (2023).

Figure 2: The location of the trial embankment showing (a) a plan of the embankment and the location of instrumentation, (b) the site location (52°11'17"N, 1°20'25"W) within the outcrop of the Charmouth Mudstone Formation in central England.

Figure 3: The ground profile derived from HS2 ground investigation data obtained beneath or near the trial embankment, showing (a) the geological profile shown in borehole strata descriptions, (b) the moisture content (%) profile, (c) the plasticity index (%) profile, (d) the specific volume profile, (e) the bulk density (kN/m^3) profile and (f) the undrained shear strength (kPa) profile from unconsolidated undrained triaxial tests. Data from the Charmouth Mudstone Formation in Oxfordshire (Briggs et al. 2022) are shown for comparison.

Figure 4: Total pressure (kPa) measured beneath the centre of the embankment (PC1) and beneath the edge of the embankment crest (PC2) using total earth pressure cells during embankment construction (November to December 2020).

Figure 5: The change in embankment height with time, back-calculated from cell pressure measurements (PC1 & PC2) and the known embankment height from drone survey measurements at PC1.

Figure 6: The relative displacement between extensometer anchors installed at various depths during construction of the trial embankment at (a) EXT1 and (b) EXT2. Note that the extensometer anchors were not equally spaced.

Figure 7: Downhole geophysical measurements of (a) shear wave velocity (m/s) and (b) compression wave velocity (m/s), at four boreholes (DHGEO_2, DHGEO_3, DHGEO_6 & DHGEO_7) located to the south of the trial embankment.

Figure 8: The maximum shear modulus profile (G_{max}) derived from the downhole geophysical measurements. The Vardanega & Bolton (2013) model for fine-grained soils, plotted using the specific volume of the triaxial data (Figure 3), is shown for comparison. Linear regressions for G_{max} are shown for the weathered clay (0 to 8mbgl) and the transition to less-weathered clay and mudstone below (9-20 mbgl).

Figure 9: The geometry parameters for the distributed vertical embankment loading equations described in Poulos & Davis (1974).

Figure 10: A normalised secant shear modulus reduction curve with strain for layers beneath the trial embankment, derived from monitoring data. These are compared to results from the Vardanega & Bolton (2013) model for fine-grained soils with plasticity indices (I_p) of 5% to 35%.

Figure 11: The average vertical stress (σ_z) vs strain (ε_z) within the soil layers beneath the trial embankment, for eight loading stages, shown for (a) near surface layers (0 to 5 mbgl) at strains approaching yield and (b) deeper layers (2.5 to 20 mbgl) at medium strains.

Figure 12: The secant shear modulus, G (MPa) vs shear strain, γ (%), for layers within the ground profile beneath the embankment. For comparison, a best-fit curve from the Vardanega & Bolton (2013) database is shown for the mean values for fine-grained soils (where I_p= 39%, p'=209 kPa, G_{max} = 68 MPa).

Figure A 1: Influence factors (points) from the Perloff et al. (1967) chart and fitted linear regressions (solid lines). The dashed line shows the fit for a 22.5^o slope angle.

Figure B 1: A normalised secant shear modulus reduction curve with strain for layers beneath the trial embankment, derived from monitoring data and assuming v_u equal to 0.458. These are compared to results from the Vardanega & Bolton (2013) model for fine-grained soils with a plasticity index (Ip) of 5% to 35%.

Table 1: Instrumentation installed beneath the trial embankment (see Figure 2).

Table 2: The extensometer anchor displacements at various depths within EXT 1 and EXT2, relative to the base anchor (mm). The measurements are shown to 1 decimal place for dates corresponding to eight known embankment loading stages.

Table 3: The relative displacement between extensometer anchors installed at various depths within EXT1 and EXT2 (mm). The measurements are shown to 1 decimal place for dates corresponding to eight known embankment loading stages. Note that the extensometer anchors were not equally spaced.

Tables

Table 1: Instrumentation installed beneath the trial embankment (see Figure 2).

Measurement type	**Instrument type (& model)**	**Instrument location & depth (mbgl)**	**Measuring range/resolution**
Total pressure (kPa)	Vibrating wire total earth pressure cell* (LPTPC09-V-LP)	PC1 at 0.3 PC2 at 0.3	A 31.7 cm diameter cell calibrated to measure pressure between 0 and 175 kPa, logged at 0.1 kPa resolution
Pore water pressure (kPa)	Vibrating wire piezometers* (VW2100)	PIEZO1 at 10, 20, 34 PIEZO2 at 7.5, 15, 25 (note: not shown in analyses)	Pore pressure between 0 and 350 kPa (at 10, 20 m) Pore pressure between 0 and 700 kPa (All others) Measurements logged at 0.1 kPa resolution
Vertical ground displacement (mm)	Vibrating wire inline extensometers (EXINLINE-1100)	EXT1 at 0, 5 10, 20, 30, 40 & 60 EXT2 at 0, 2.5, 7.5, 15, 25, 35 & 50	Tape measurement at 0.02 mm resolution

* Calibrated by the manufacturer in compliance with BS EN ISO/IEC 17025:2017 (British Standards Institution, 2017)

Table 2: The extensometer anchor displacements at various depths within EXT 1 and EXT2, relative to the base anchor (mm). The measurements are shown to 1 decimal place for dates corresponding to eight known embankment loading stages.

Stage	**Date & time**	**Emb. Height (m)**		**Anchor displacement relative to the base anchor (mm to 1dp)**													
			Anchor location	**EXT1**	**EXT1**	**EXT1**	**EXT1**	**EXT1**	**EXT1**	**EXT1**	**EXT2**	**EXT2**	**EXT2**	**EXT2**	**EXT2**	**EXT2**	**EXT2**
			Anchor depth (mbgl)	**60**	**40**	**30**	**20**	**10**	**5**	**0**	**50**	**35**	**25**	**15**	**7.5**	**2.5**	**0**
1	07/11/2020 (18:00)	1.16		0.0	-0.4	-0.4	-0.4	-0.4	-0.5	-4.3	0.0	0.0	0.0	-0.1	-0.3	-0.5	-6.0
2	20/11/2020 (18:00)	3.69		0.0	-0.2	-0.4	-0.7	-1.1	-1.5	-16.6	0.0	0.0	-0.1	-0.5	-1.4	-2.1	-16.1
3	23/11/2020 (18:00)	4.33		0.0	-0.4	-0.7	-1.1	-1.8	-2.4	-21.5	0.0	0.0	-0.1	-0.7	-1.9	-3.0	-22.7
4	26/11/2020 (18:00)	4.82		0.0	-0.9	-1.3	-1.8	-2.8	-3.5	-27.5	0.0	0.0	-0.1	-1.1	-2.7	-4.0	-32.3
5	27/11/2020 (18:00)	5.45		0.0	-1.0	-1.4	-1.9	-3.1	-3.9	-29.3	0.0	0.0	-0.2	-1.2	-3.0	-4.6	-35.4
6	30/11/2020 (18:00)	5.86		0.0	-0.3	-0.7	-1.4	-2.8	-3.8	-31.8	0.0	0.0	-0.2	-1.4	-3.8	-5.7	-42.3
7	02/12/2020 (18:00)	6.59		0.0	-0.2	-0.7	-1.5	-3.2	-4.4	-34.8	0.0	0.0	-0.2	-1.6	-4.7	-7.0	-49.7
8	09/12/2020 (18:00)	8.23		0.0	-0.3	-0.9	-2.0	-4.3	-6.1	-43.8	0.0	0.0	-0.3	-2.3	-5.7	-9.6	-57.9

Table 3: The relative displacement between extensometer anchors installed at various depths within EXT1 and EXT2 (mm). The measurements are shown to 1 decimal place for dates corresponding to eight known embankment loading stages. Note that the extensometer anchors were not equally spaced.

Stage	**Date & time**	**Emb. Height (m)**		**Relative displacement between the extensometer anchors (mm to 1dp)**												
			Anchor location	**EXT1**	**EXT1**	**EXT1**	**EXT1**	**EXT1**	**EXT1**		**EXT2**	**EXT2**	**EXT2**	**EXT2**	**EXT2**	**EXT2**
			Anchor depths (mbgl)	**40-60**	**30-40**	**20-30**	**10-20**	**5-10**	**0-5**		**35-50**	**25-35**	**15-25**	**7.5-15**	**2.5-7.5**	**0-2.5**
1	07/11/2020 (18:00)	1.16		-0.4	0.0	0.0	0.0	0.0	-3.8		0.0	0.0	0.0	0.0	0.0	-5.5
2	20/11/2020 (18:00)	3.69		0.0	0.0	-0.3	-0.5	-0.4	-15.1		0.0	0.0	-0.4	-0.9	-0.8	-14.0
3	23/11/2020 (18:00)	4.33		-0.4	-0.3	-0.4	-0.7	-0.6	-19.2		0.0	0.0	-0.6	-1.2	-1.1	-19.7
4	26/11/2020 (18:00)	4.82		-0.9	-0.4	-0.5	-1.0	-0.7	-24.0		0.0	0.0	-0.9	-1.6	-1.4	-28.3
5	27/11/2020 (18:00)	5.45		-1.0	-0.4	-0.6	-1.2	-0.8	-25.4		0.0	0.0	-1.0	-1.8	-1.6	-30.8
6	30/11/2020 (18:00)	5.86		-0.3	-0.5	-0.7	-1.4	-1.0	-28.0		0.0	0.0	-1.2	-2.4	-1.9	-36.6
7	02/12/2020 (18:00)	6.59		0.0	-0.5	-0.8	-1.6	-1.2	-30.4		0.0	0.0	-1.4	-3.1	-2.3	-42.7
8	09/12/2020 (18:00)	8.23		-0.3	-0.6	-1.1	-2.3	-1.8	-37.7		0.0	-0.3	-2.0	-3.5	-3.9	-48.4

Figures

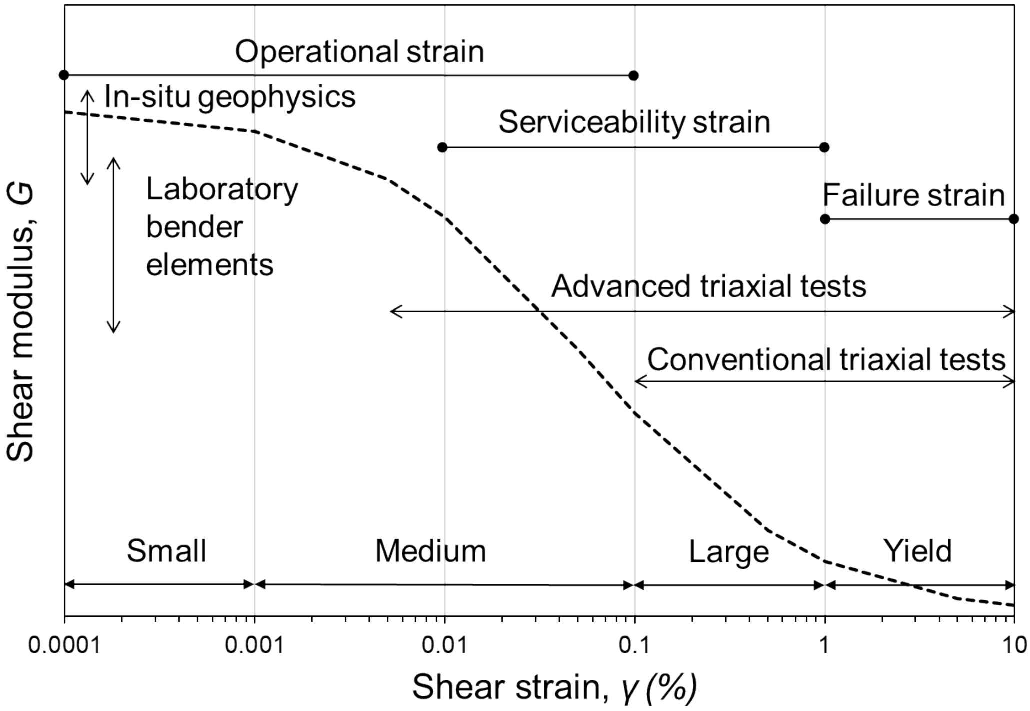

Figure 1: A shear stiffness reduction curve showing the typical strain range for geotechnical structures, analysis types and the approximate range of different measurement methods. Redrawn from Mair (1993), Ishihara (1996), Atkinson (2000), Clayton (2011) and O'Brien et al. (2023).

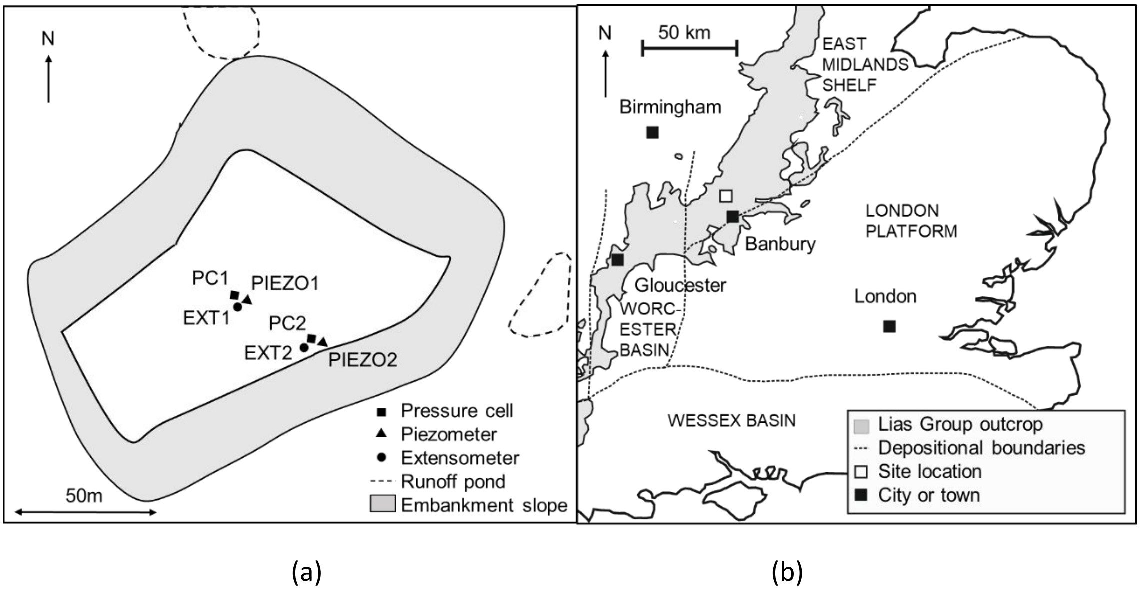

Figure 2: The location of the trial embankment showing (a) a plan of the embankment and the location of instrumentation, (b) the site location (52°11'17"N, 1°20'25"W) within the outcrop of the Charmouth Mudstone Formation in central England.

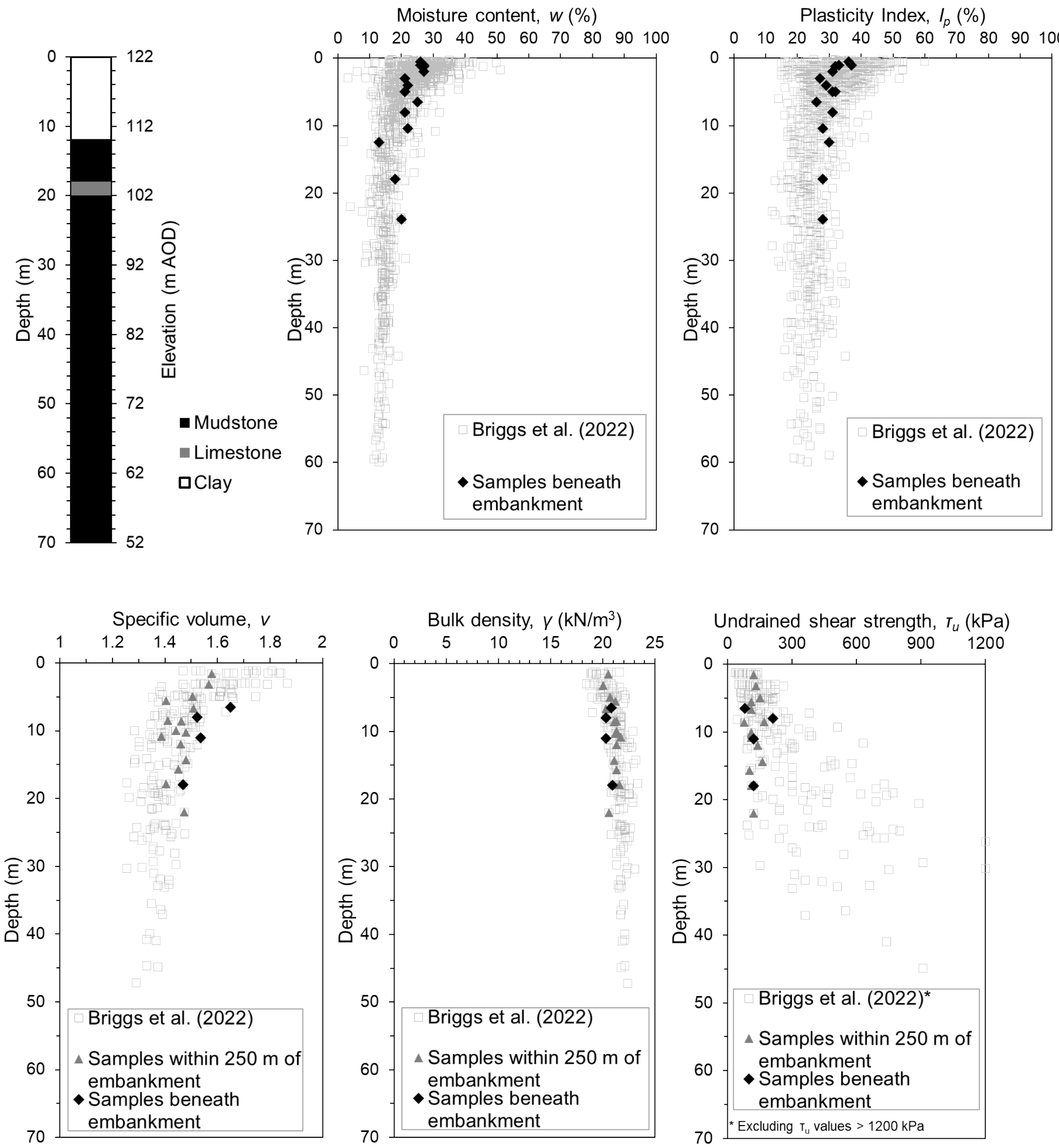

Figure 3: The ground profile derived from HS2 ground investigation data obtained beneath or near the trial embankment, showing (a) the geological profile shown in borehole strata descriptions, (b) the moisture content (%) profile, (c) the plasticity index (%) profile, (d) the specific volume profile, (e) the bulk density (kN/m^3) profile and (f) the undrained shear strength (kPa) profile from unconsolidated undrained triaxial tests. Data from the Charmouth Mudstone Formation in Oxfordshire (Briggs et al. 2022) are shown for comparison.

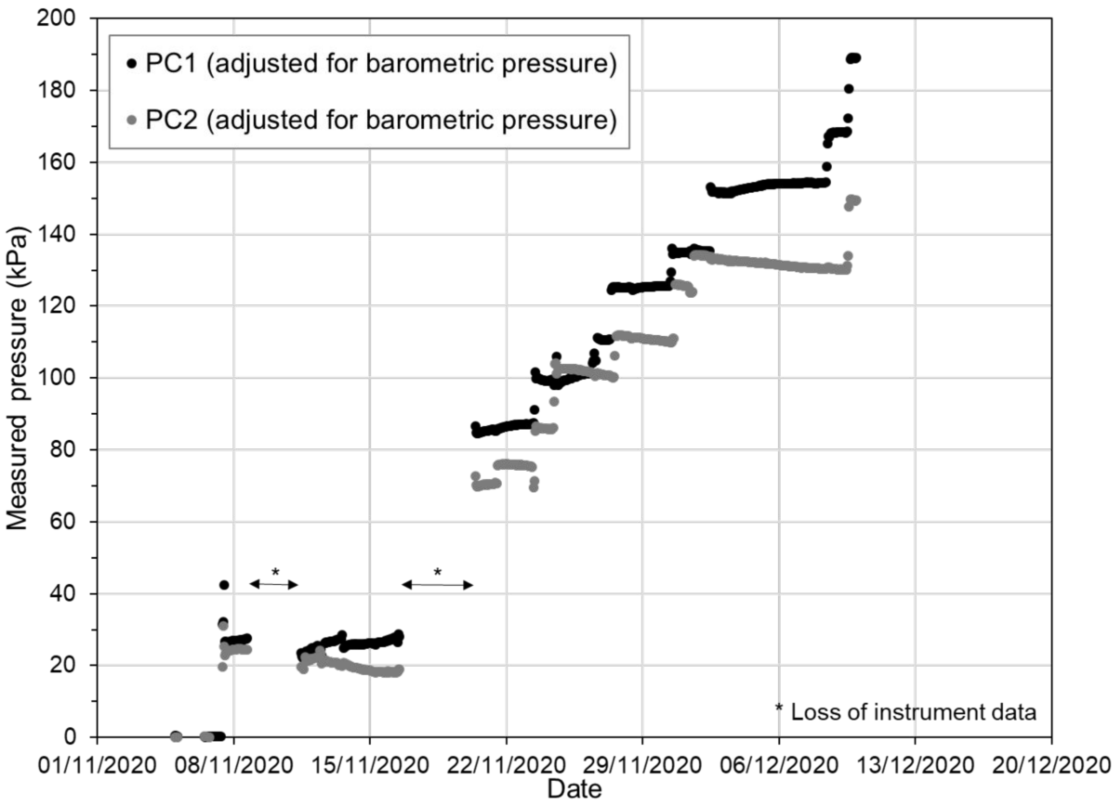

Figure 4: Total pressure (kPa) measured beneath the centre of the embankment (PC1) and beneath the edge of the embankment crest (PC2) using total earth pressure cells during embankment construction (November to December 2020).

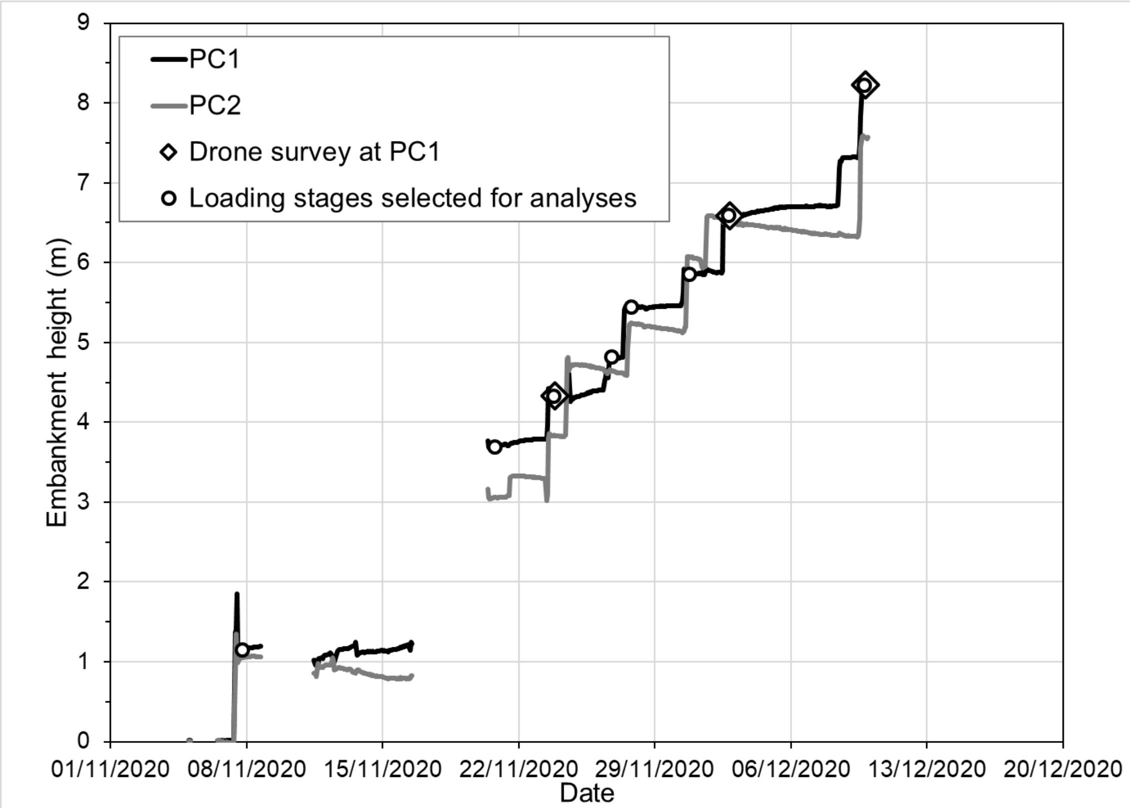

Figure 5: The change in embankment height with time, back-calculated from cell pressure measurements (PC1 & PC2) and the known embankment height from drone survey measurements at PC1.

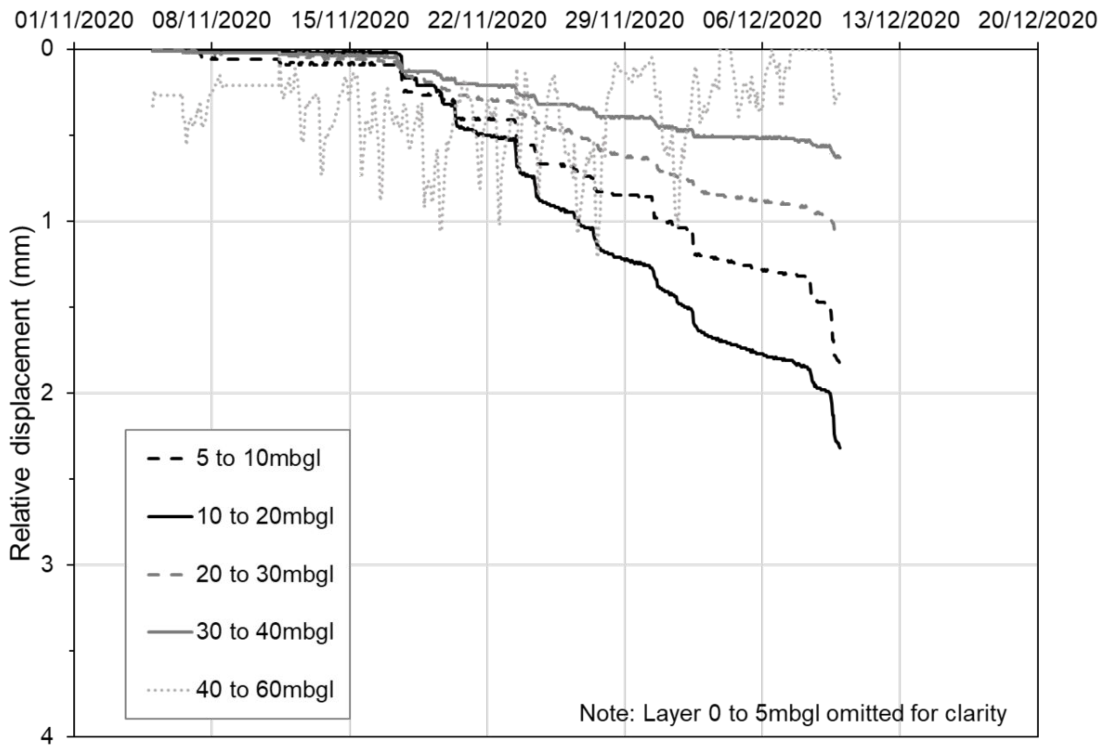

(a)

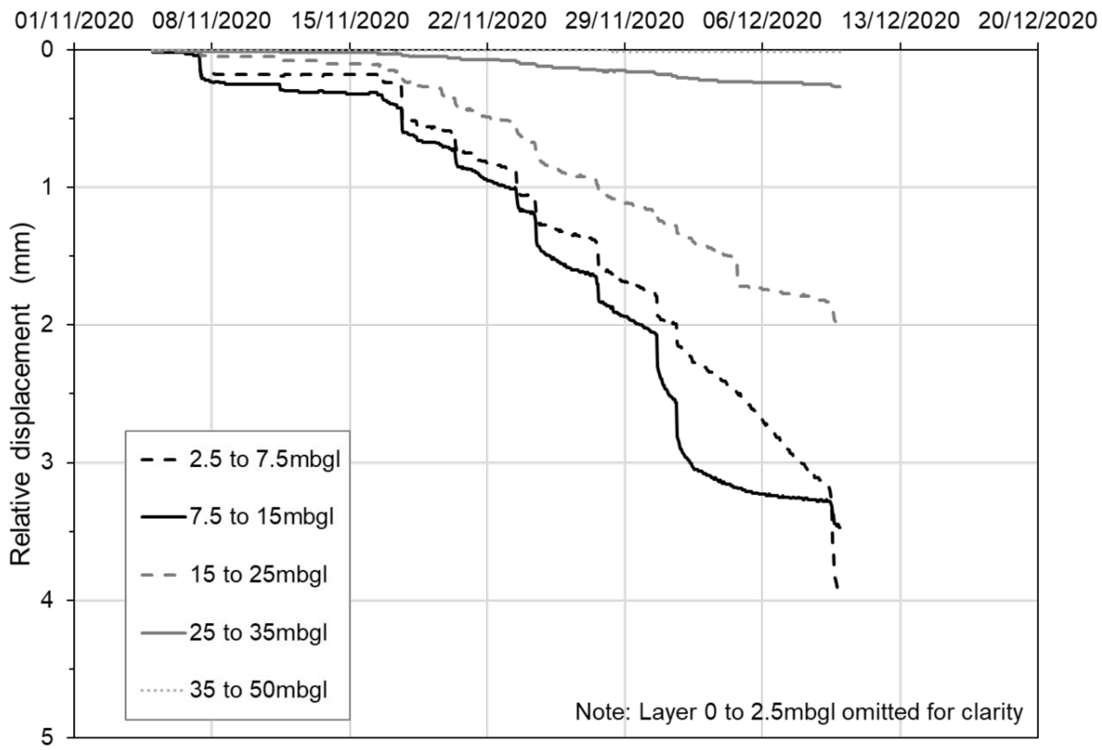

(b)

Figure 6: The relative displacement between extensometer anchors installed at various depths during construction of the trial embankment at (a) EXT1 and (b) EXT2. Note that the extensometer anchors were not equally spaced.

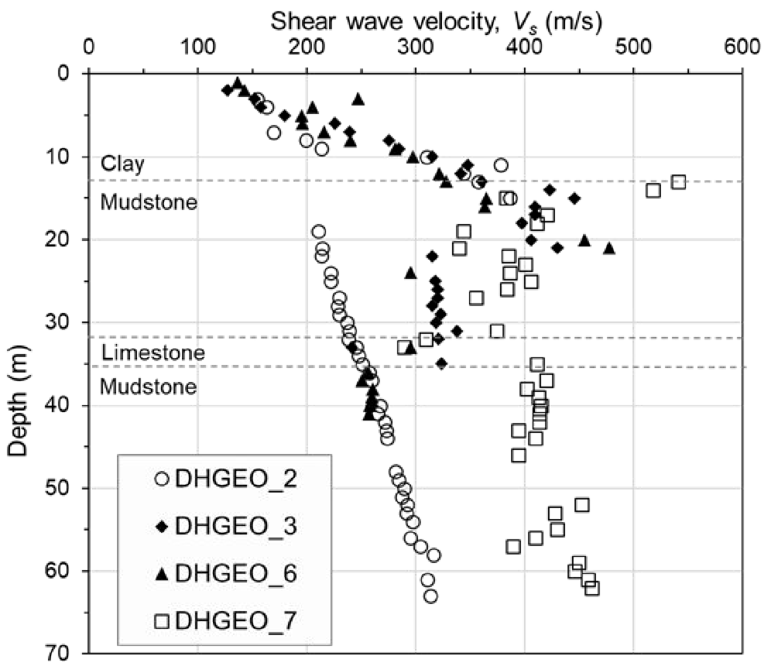

(a)

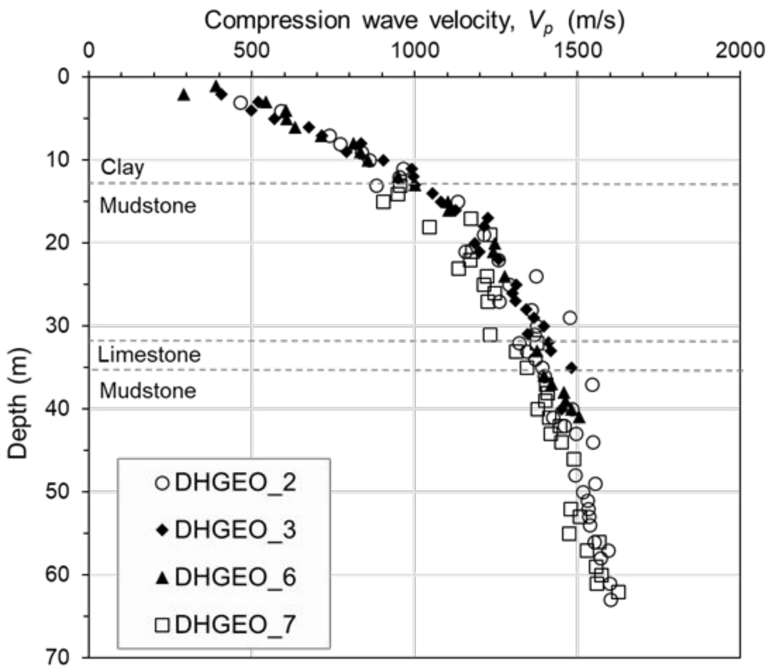

(b)

Figure 7: Downhole geophysical measurements of (a) shear wave velocity (m/s) and (b) compression wave velocity (m/s), at four boreholes (DHGEO_2, DHGEO_3, DHGEO_6 & DHGEO_7) located to the south of the trial embankment.

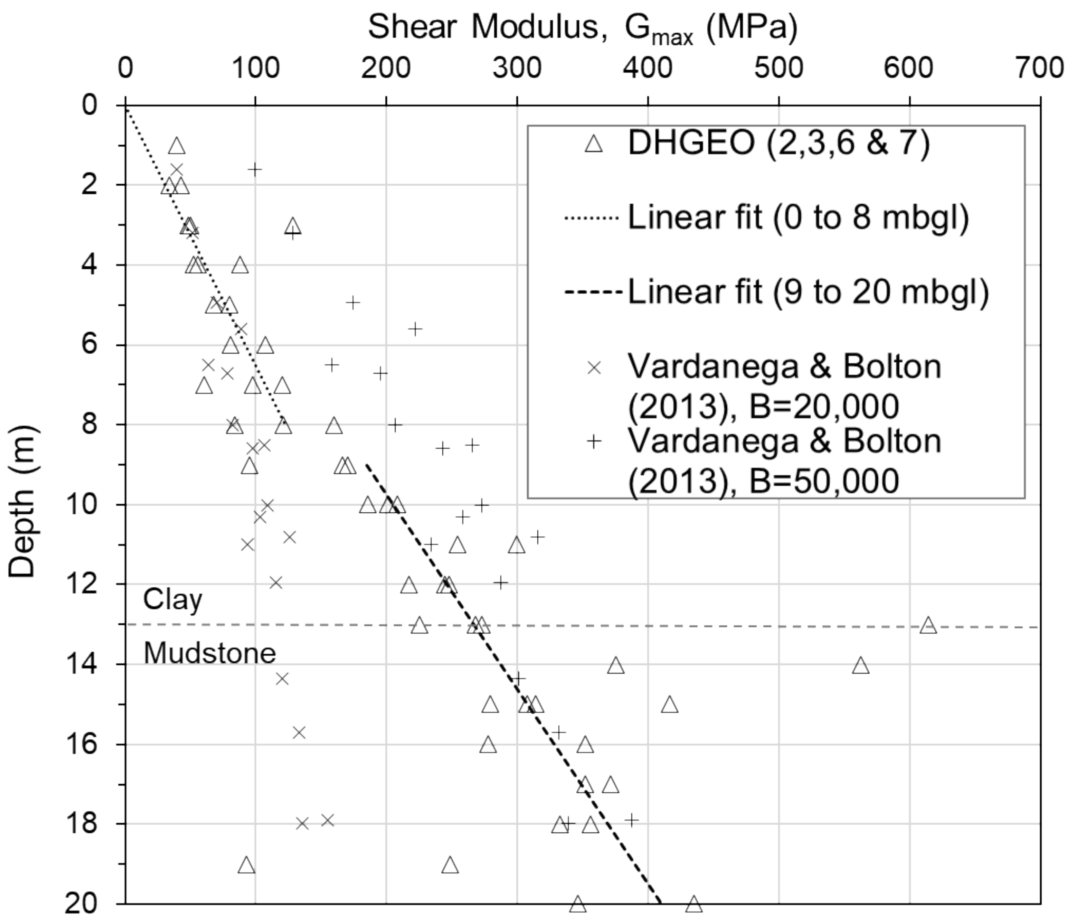

Figure 8: The maximum shear modulus profile (G_{max}) derived from the downhole geophysical measurements. The Vardanega & Bolton (2013) model for fine-grained soils, plotted using the specific volume of the triaxial data (Figure 3), is shown for comparison. Linear regressions for G_{max} are shown for the weathered clay (0 to 8mbgl) and the transition to less-weathered clay and mudstone below (9-20 mbgl).

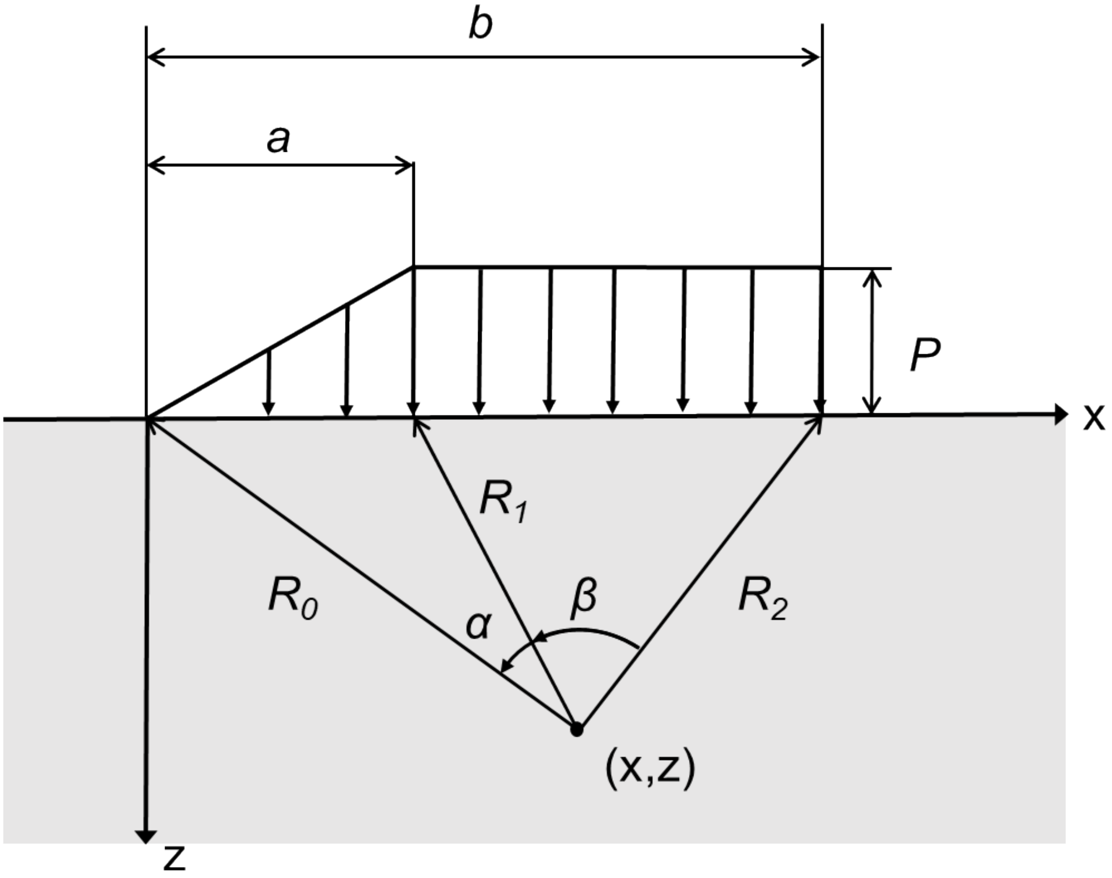

Figure 9: The geometry parameters for the distributed vertical embankment loading equations described in Poulos & Davis (1974).

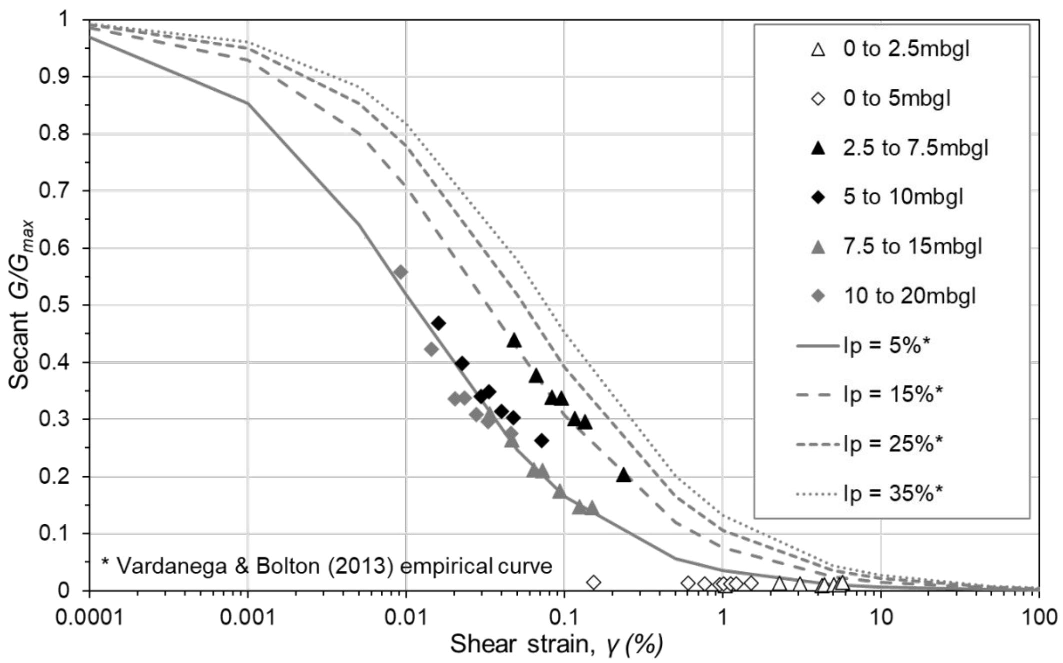

Figure 10: A normalised secant shear modulus reduction curve with strain for layers beneath the trial embankment, derived from monitoring data. These are compared to results from the Vardanega & Bolton (2013) model for fine-grained soils with plasticity indices (I_p) of 5% to 35%.

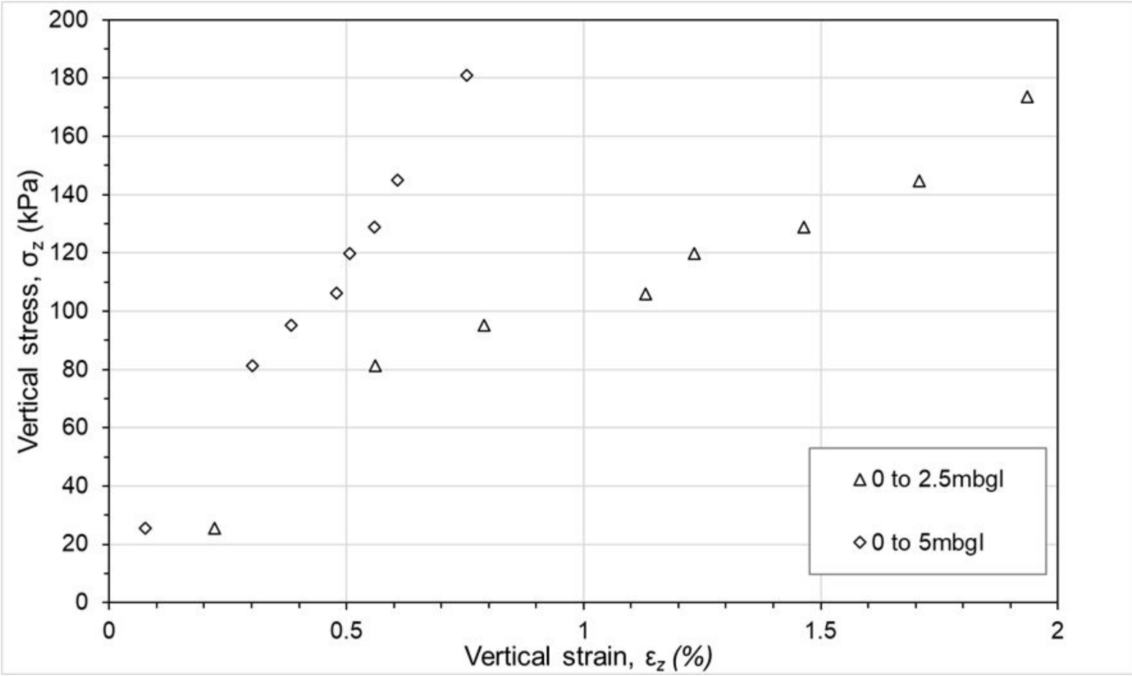

(a)

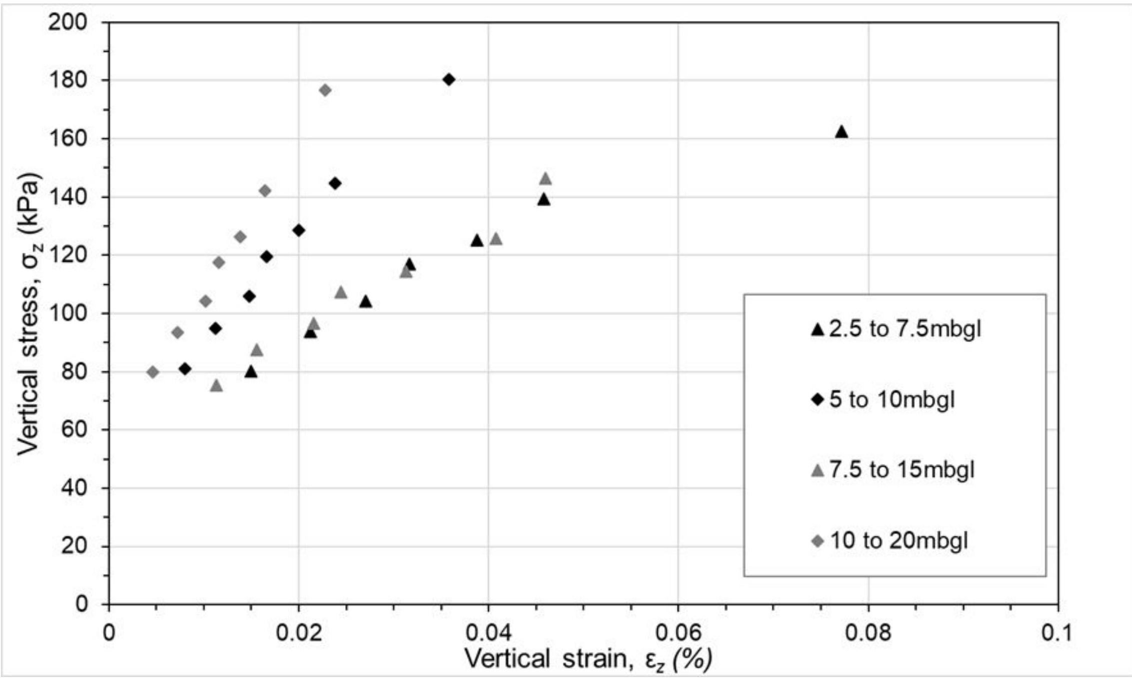

(b)

Figure 11: The average vertical stress (σ_z) vs strain (ε_z) within the soil layers beneath the trial embankment, for eight loading stages, shown for (a) near surface layers (0 to 5 mbgl) at strains approaching yield and (b) deeper layers (2.5 to 20 mbgl) at medium strains.

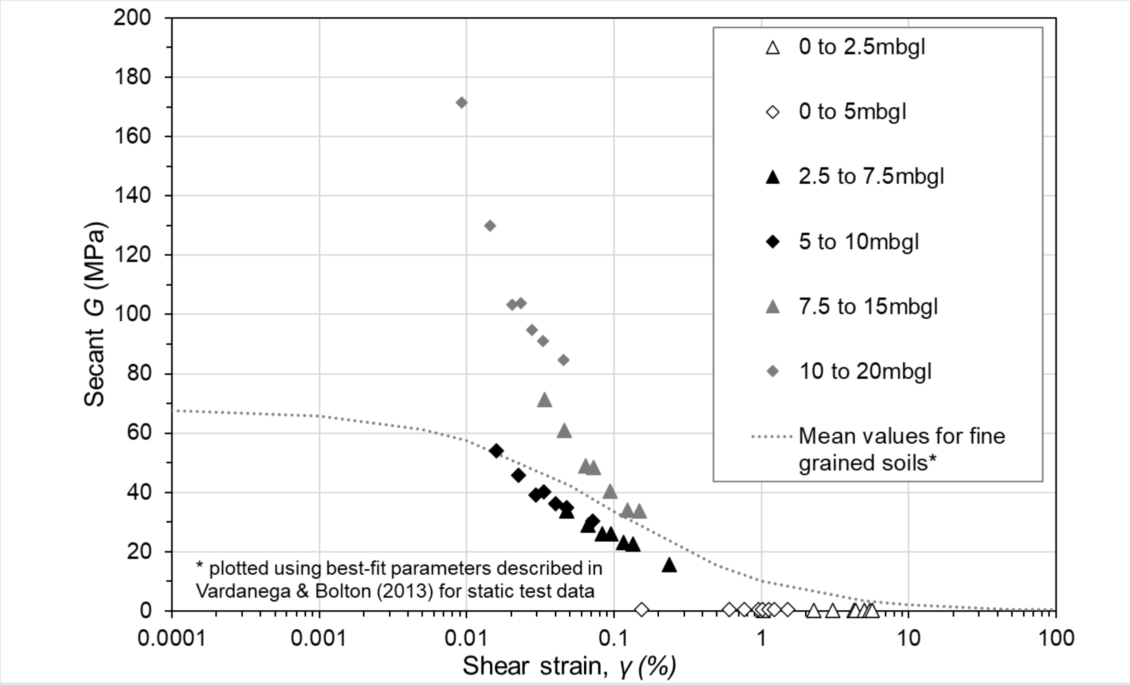

Figure 12: The secant shear modulus, G (MPa) vs shear strain, γ (%), for layers within the ground profile beneath the embankment. For comparison, a best-fit curve from the Vardanega & Bolton (2013) database is shown for the mean values for fine-grained soils (where I_p= 39%, p'=209 kPa, G_{max} = 68 MPa).

Appendix A

Pressure cell PC2 was installed beneath the edge of the embankment crest and was influenced by its proximity to the embankment slope. Elastic solutions for stresses at the base of an embankment, as presented by Perloff et al. (1967) were used to quantify the influence of the embankment slope on the measured stresses. These solutions link the embankment height at each loading stage (H), embankment crest width L and distance to the embankment centre line (x) to the predicted influence factor ($I_z = \sigma_z/(H\gamma_{emb})$). Perloff et al. (1967) presented solutions for $\nu = 0.3$ and various slope angles ($\theta =$ 15, 30, 45 and 60 degrees) and crest widths (L/H = 0, 0.5, 1, 3 and 5) in chart form. The x-location of PC2 in Perloff's coordinate system is given by:

$$\frac{x}{H} = \frac{L}{H} + \frac{1}{\tan\theta}\left[\frac{H_{final}}{H} - 1\right]$$

Equation A 1

Where H_{final} is the final embankment height, i.e. 8.2 m

The Perloff et al. (1967) charts were digitised for $L/H = 5$ and for $\theta = 15$ and θ = 30 degrees. The influence factors for PC2 were subsequently determined. The results (Figure A 1) show that when the embankment height is still relatively low, measured stresses in PC2 will not be affected by the embankment slope. However, the influence factors reduced in almost linear fashion beyond a certain embankment height threshold. As the embankment had a slope angle close to 22.5 degrees (halfway between the 15- and 30-degree cases), the intercepts and slopes of the fits for the 15 and 30 degree data were averaged. This resulted in:

$$I_z = \frac{\sigma_z}{\gamma_{emb}H} = \min\begin{cases} 1 \\ 1.134 - 0.275\,\dfrac{H}{H_{final}} \end{cases}$$

Equation A 2

This is shown in Figure A 1.

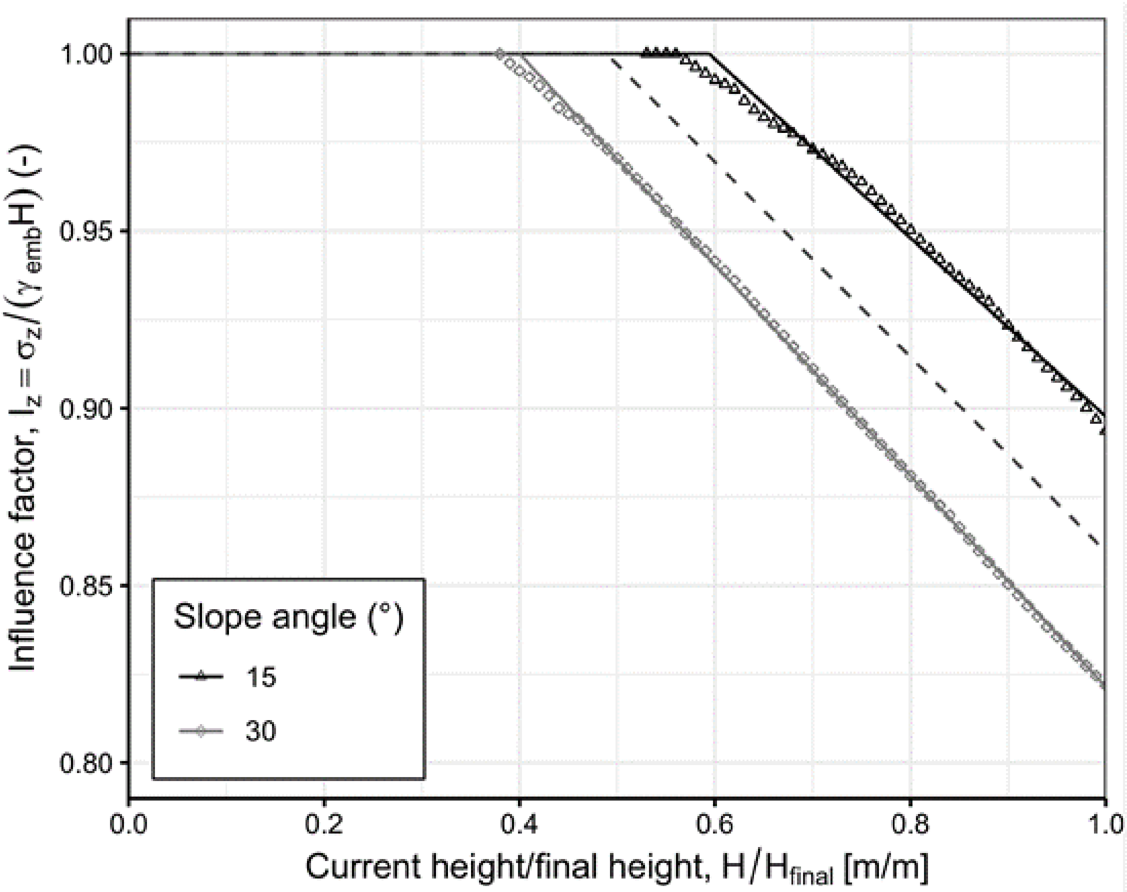

Figure A 1: Influence factors (points) from the Perloff et al. (1967) chart and fitted linear regressions (solid lines). The dashed line shows the fit for a 22.5° slope angle.

Appendix B

The interpretation of the measurements beneath the trial embankment assumed fully undrained conditions, with no volume change (i.e. v_u = 0.5). However, Briggs et al. (2024) showed that Skempton's (1954) *B* value can reduce below unity in genuinely undrained conditions in stiff clays and mudstones such as those of the Charmouth Mudstone Formation. This is because their high stiffness relative to that of water makes the *B* values sensitive to very small reductions of the in-situ saturation ratio. For example, a small reduction in saturation ratio to 0.995 (i.e. 99.5%) can reduce the *B* value from unity to 0.2. The influence of the *B* value on the undrained Poisson's Ratio (v_u) can be calculated using:

$$v_u = \frac{3v + B(1-2v)}{3 - B(1-2v)}$$

Equation B 1

Briggs et al. (2024) showed that *B* values beneath the trial embankment were approximately 0.6 during construction. A drained Poisson's Ratio (v) was estimated as 0.4. Figure B1 shows the data replotted with the assumptions that B = 0.6, v = 0.4 and therefore v_u = 0.458. Figure B 1 shows that the data from the shallower layers (black symbols) move up (i.e. higher G/G_{max}) and to the left (i.e. lower shear strain) relative to their positions when v_u = 0.5 (Figure 10). The deeper layers (grey symbols) are less affected and remain close to the Vardanega & Bolton (2013) curve fit for I_p = 5%.

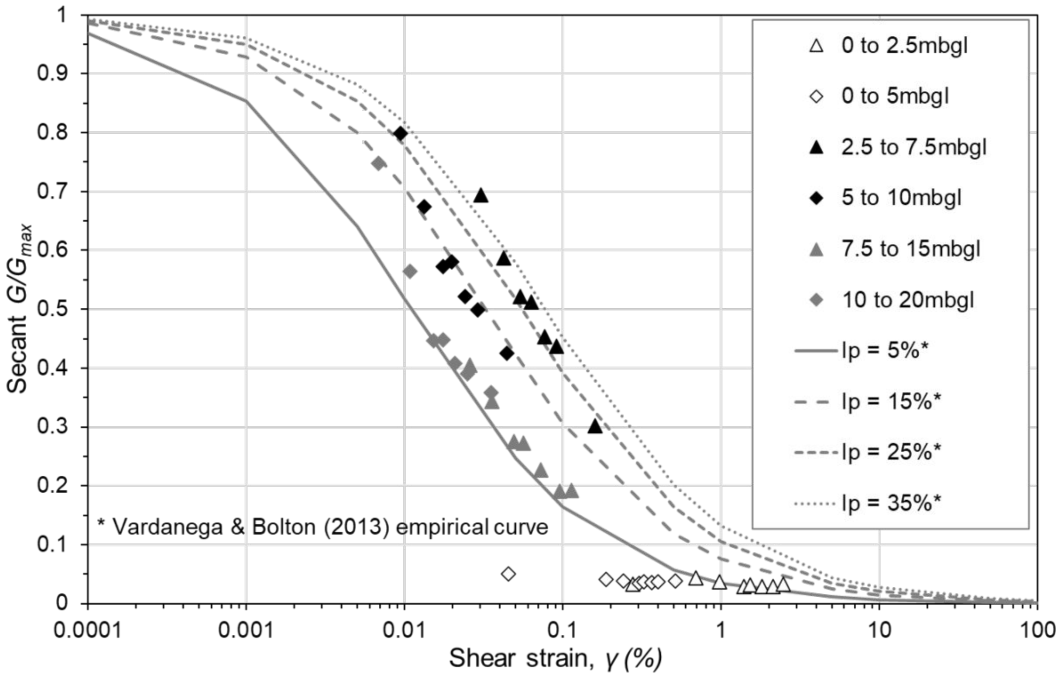

Figure B 1: A normalised secant shear modulus reduction curve with strain for layers beneath the trial embankment, derived from monitoring data and assuming v_u equal to 0.458. These are compared to results from the Vardanega & Bolton (2013) model for fine-grained soils with a plasticity index (Ip) of 5% to 35%.